Quantitative Imaging of the Air-Water Flow Fields Formed by Unsteady Breaking Waves

by

Jesse Belden

Submitted to the Department of Mechanical Engineering
in partial fulfillment of the requirements for the degree of

Master of Science in Mechanical Engineering

at the

MASSACHUSETTS INSTITUTE OF TECHNOLOGY

February 2009

Author .....
Department of Mechanical Engineering
January 16, 2009

Certified by .....
Alexandra H. Techet
Associate Professor of Mechanical and Ocean Engineering
Thesis Supervisor

Accepted by .....
David E. Hardt
Ralph E. and Eloise F. Cross Professor of Mechanical Engineering
Chairman, Department Committee on Graduate Students

Quantitative Imaging of the Air-Water Flow Fields Formed by Unsteady Breaking Waves

by

Jesse Belden

Submitted to the Department of Mechanical Engineering
on January 16, 2009, in partial fulfillment of the
requirements for the degree of
Master of Science in Mechanical Engineering

Abstract

An experimental method for simultaneously measuring the velocity fields on the air and water side of unsteady breaking waves is presented. The method is applied to breaking waves to investigate the physics of the air and water flow fields to further our knowledge of the impact of wave breaking on air–sea interaction. The method includes a novel technique for seeding the air flow such that the air velocity can be resolved in the absence of wind. Low density particles which have large Stokes drag and ability to respond to high frequency flow fluctuations are used to seed the air flow. Multi–camera, multi–laser particle image velocimetry (PIV) setups are applied to small-scale shoaling breaking waves, yielding fully time–resolved velocity fields. The surface tension of the fluid is altered and controlled to form both spilling and plunging breaking waves. Application of the developed experimental method to these breaking waves reveals interesting flow physics in the air and water. Results for the velocity and vorticity fields on the water side show qualitative agreement to published data, and comparisons are drawn where applicable. Quantitative experimental data for the air flow induced by wave breaking in the absence of wind has not previously been observed, to the author's knowledge. Revealing physical insights and observations are drawn from this novel data.

Thesis Supervisor: Alexandra H. Techet
Title: Associate Professor of Mechanical and Ocean Engineering

Acknowledgments

First and foremost, I must acknowledge my adivsor, Professor Alexandra Techet. Her vision for this project and support throughout has helped to create a stimulating environment which encourages questioning and progress. Also, her patience and understanding of the need for a balanced life is appreciated and does not go unnoticed.

I also greatly appreciate the patience and support of my loving wife, Mary. Many long nights and weekend days she has understood my need to disappear to the lab, and on many occasions has ventured with me. She has taken a genuine interest in my research, for which I am grateful if not somewhat confused. I also admire her diligent and dedicated career as an English teacher, and realize how lucky I am as an engineer to have a wonderful editor–in–chief. Finally, I would be remiss if I did not apologize for so many frozen dinners; I'm sorry, only a few more years...

Finally, I need to acknowledge my family. My Mom and Dad's parental, professional and financial support have made it possible for me to be here today. And to my brother, Calum, who could care less about vortex rings and turbulence, his humor about my work helps me keep it all in perspective.

THIS PAGE INTENTIONALLY LEFT BLANK

Contents

List of Figures

List of Tables

THIS PAGE INTENTIONALLY LEFT BLANK

Chapter 1

Introduction

Given the visual complexity of breaking waves on the ocean's surface, it is perhaps not surprising that they play an important part in many complex ocean phenomena. The study of wave breaking is old, and yet knowledge is far from complete due to the highly nonlinear nature of the fluid flow. The painting done by Winslow Homer in 1883 shown in Figure 1-1, entitled *Incoming Tide, Scarboro Maine* [16], depicts many of the complex phenomena associated with wave breaking. The large breaking wave that catches the observer's eye appears to be the result of wave–wave interaction between waves reflecting from the shore and incoming waves. A large spray shoots up from the breaker, forming droplets and interacting with the air above. Breaking waves also pound the rocks, eroding the shore that likely has receded since Homer eternalized the Maine coast. In the right of the painting the peaks of smaller – perhaps spilling – breakers roughen the ocean's surface. Crashing, foaming, mixing and eroding; all depicted in this rich work by Homer, and all the work of breaking waves. Interestingly enough, images are used extensively in the study of wave breaking. Nowadays, the images are used for quantifying the water and air flow fields associated with breaking, and that is the purpose of this thesis. However, quantitative images reveal the physics associated with much of what Homer's painting shows, as the complex nature he captured has proven elusive to fully describe theoretically, computationally and even experimentally.

Figure 1-1: Painting by Winslow Homer entitled *Incoming Tide, Scarboro Maine*, [16],

1.1 Background & Motivation

Scientific interest and engineering applications have stimulated extensive study of breaking waves through the decades. The breaking process limits the amplitude of waves and dissipates energy carried by waves ([35], [27]). Breaking waves also provide a mechanism for the transfer of momentum and energy from the wind to the near surface fluid flow ([35], [27], [21]); this leads the formation of surface currents and the production of near-surface turbulence. Oceanographers and biologists are interested in breakers because, in shallow waters, the flow induced by wave breaking can affect plants and sediment on the ocean floor ([10]). Knowledge of breaking waves is critical for ship and offshore engineering applications because the loading imposed by breakers is significant ([35]). Also, breaking waves are generated by ships, and create a bubbly wake and contribute to drag on the ship ([10]). More relevant to the present study is the fact that breaking waves contribute to the air-sea transfer of mass, momentum, heat and energy at the ocean surface, and play a significant role in absorption of gas at the air-sea interface ([27]).

Before delving further into the influence of wave breaking on air-sea interaction,

it is important to discuss why waves break and what constitutes a breaking wave. Breaking waves can be classified as steady or unsteady, with the former referring to a transient event, and the latter referring to an event that is constant in time. Unsteady breakers are generated due to wave-wave, wave-current or wind-wave interaction ([10]). Steady breakers occur when a sustained energy input exists, as in the case of a ship wave or a wave induced by a current flowing over a submerged object ([10]). Svendsen [40] describes a classification which groups breakers into three types: spilling breakers, plunging breakers and surging breakers. Spilling breakers (described in Svendsen [40] and extensively in Duncan [10]) are characterized by an asymmetric crest, with a bulge on the top and front of the crest. The top image in Figure 1-2 shows the geometric features of spilling breakers as defined in Qiao & Duncan [33]. The bulge meets the crest in a sharp corner called the toe, and forward of the toe a capillary wave train exists. During the breaking process, the toe moves down the front face of the wave and vorticity is generated beneath the bulge. This quickly develops into a turbulent flow in the crest, but the turbulence is usually confined to the near-surface region. Spilling breakers typically do not result in significant air entrainment. Although spilling breakers are more common on the open ocean, plunging breakers are likely more recognizable to the beach goer. Plungers are characterized by a very steep front face of the wave, from which a fluid jet emanates. The jet, under the influence of gravity, "plunges" into the trough preceding the breaker, generating significant turbulence and entraining air. The top image in Figure 1-3 shows computational results shown in Peregrine [31] that demonstrate the formation of the characteristic jet of a plunger. Surging breakers occur in nearshore region on very shallow water. For these breakers, the front of the crest becomes very steep, then the bottom of the crest projects forward along the shore. Not as much turbulence is generated for surging breakers as for the spillers and plungers.

Although the present work focuses on wave breaking in the context of air-sea interaction, many theoretical, computational and experimental studies of wave breaking have been carried out to reveal the underlying physics and examine a variety of applications. Duncan [10] provides a review of work done in the area of spilling breakers.

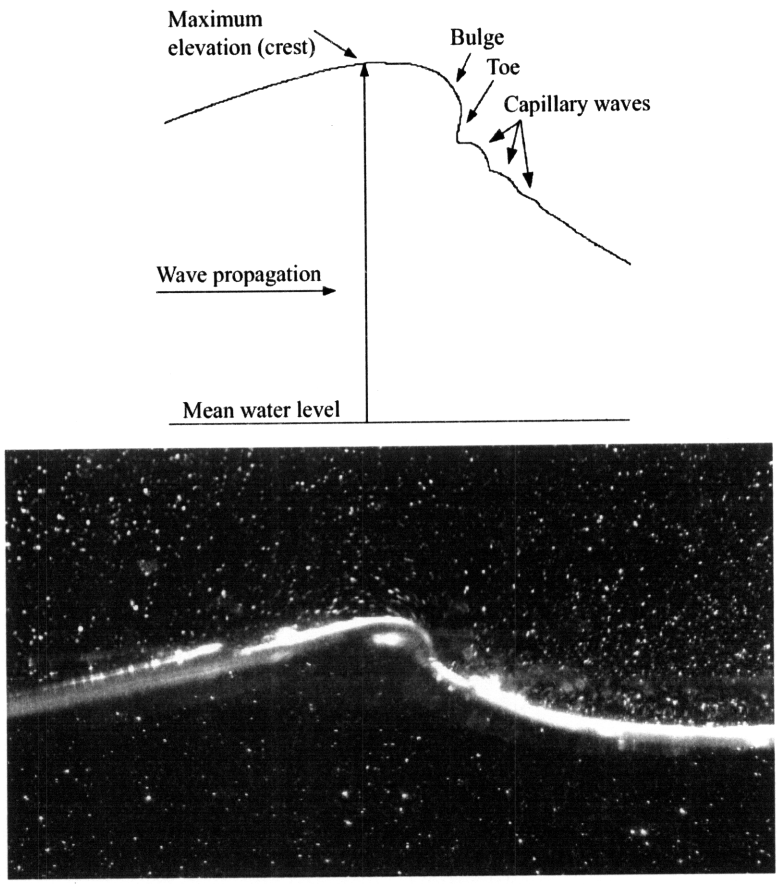

Figure 1-2: Top image is a schematic of a spilling breaking wave with prominent features labeled (reprinted from Qiao & Duncan [33]). Bottom image is a PIV image of a spilling breaker with water and air flow seeded from the present study.

The review includes descriptions of spiller geometry throughout breaking, the effect of surface tension on breaking and cites some of the open questions regarding the spilling breaking process. In an older review, Peregrine [31] highlights work done in the are of breaking waves on beaches. Significant attention is paid to plunging breakers in this review. Longuet-Higgins theoretically treats the generation of vorticity in spilling breakers in [22] and shear instabilities in spillers in [23]. Longuet-Higgins and Cokelet [24] perform numerical simulations to model steep waves from which a jet emanates and the surface overturns. In early experiments on the water side of the interface, Rapp & Melville [35] use wave gauges and a control volume approach to measure the loss of momentum flux and energy flux for dispersively generated spilling and plunging breaking waves. They also use laser doppler anemometry to measure

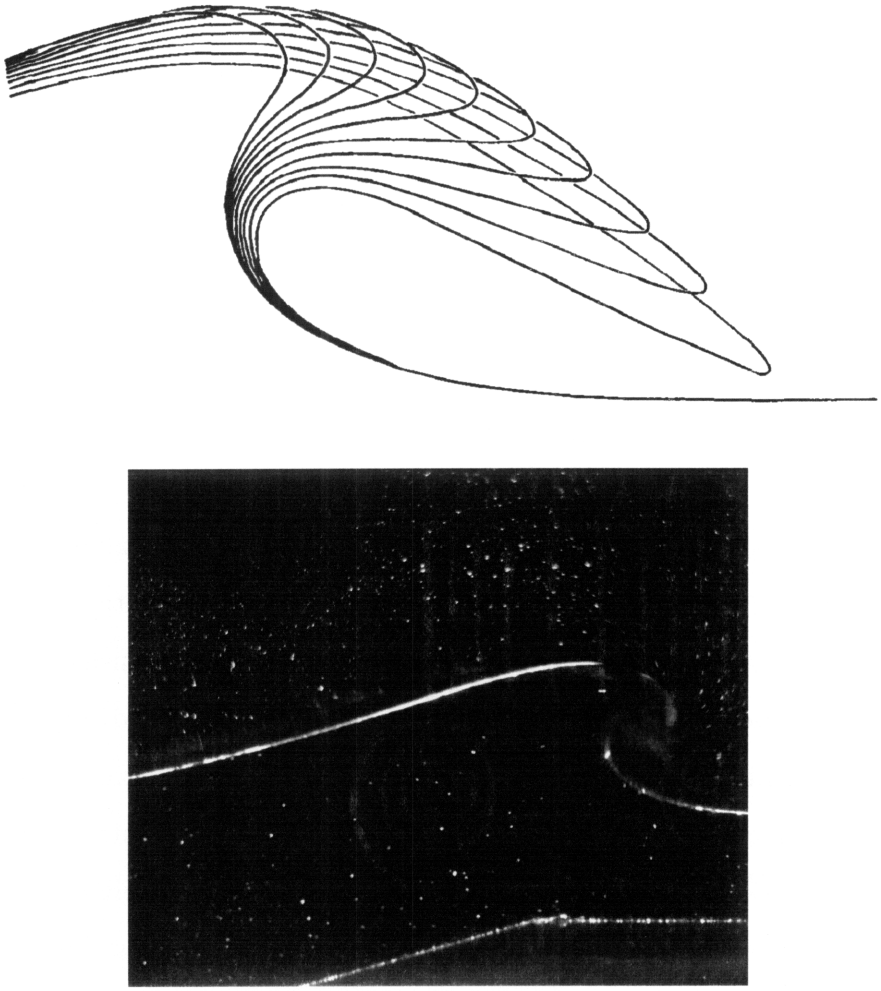

Figure 1-3: Top image is results from a computational study showing the evolution of a plunging breaker (reprinted from Peregrine [31]). Bottom image is a PIV image of a plunging breaker with water and air flow seeded from the present study.

velocities in the breaking region, and dye visualization to examine turbulent mixing for the breaking waves. More recently, Duncan et al. [11] make use of laser-induced florescence (LIF) to measure and thoroughly describe the surface geometry of spilling breaking waves. The onset of PIV has enabled more detailed quantification of the nature of the water flow in both steady (e.g., Dabiri & Gharib [8]), quasi-steady (e.g., Lin & Rockwell [20]) and unsteady breakers (e.g., Qiao & Duncan [33], Perlin et al. [32]). Turbulence statistics have also been experimentally measured for unsteady breaking waves (e.g., Melville et al. [28], Chang & Liu [5]). The near-surface properties in the water beneath microscale breaking wind-waves are resolved using PIV

by Peirson. [30], who studies velocities and stresses in the near-surface region, and by Siddiqui & Loewen [38] who investigate coherent structures in the near-surface region.

The impact of wave breaking on air-sea interaction remains an active area of research. As mentioned earlier, air-sea interaction influences the transfer of heat, mass, momentum and gas between the ocean and the atmosphere ([27]. Breaking waves play an important yet not fully understood role in this interaction. Experimental and numerical methods have developed and continue to develop revealing a more complete physical understanding of breaking waves and the air-sea interface. Melville [27] highlights the effects of wave breaking on air-sea interaction in a paper which reviews work done in the areas of wind-wave interaction, air-sea momentum flux, wave energy dissipation, surface boundary layers, and gas and heat transfer. Some of the work that considers near-surface water flow has been mentioned already. Experiments investigating flow on the air side of breaking waves also exist, although most include wind which affects the overall dynamics of the air-sea interaction. In early experimental work on the air side of the interface, Banner & Melville [3] use smoke visualization and pressure measurements to investigate the air flow shear stresses and separation over steady breaking waves in a wind-wave flume. Kawai [18] uses solid particles to visualize the air flow separation over wind waves. More recently, Reul et al. [36] perform a PIV study of the air flow separation over a mechanically generated breaking wave in the presence of wind. Small water droplets are used to seed the air flow, and the water flow is not seeded. Veron et al. [42] investigate the velcoity, vorticity and stress in the boundary layer of the air flow over wind waves using PIV with water droplets serving as the air flow seeding method.

If the effect of wave breaking on the air above is to be more thoroughly understood, it is necessary to study the air flow above breaking waves without wind. Numerical studies have begun to investigate the air flow above waves during the breaking process, in the absence of ambient wind. Chen et al. [7] use a volume-of-fluid (VOF) method to model a liquid-gas medium, and study the velocity and vorticity in the liquid side of plunging waves generated in this medium. They also consider the entrainment of gas,

but do not report velocity vectors in the gas. Hendrickson [13] investigates spilling and plunging breaking waves with a direct numerical simulation of the Navier-Stokes equations to reveal physics on both sides of the air-water interface in the absence of wind; velocity, vorticity and energy are reported for both the air and water media. A need remains for experimental quantification of the air flow above breaking waves in the absence of wind such that air flow dynamics induced by wave breaking can be elucidated. This thesis presents the details of a high-speed PIV technique which makes use of unique air flow seeding to simultaneously investigate the flow on the air and water side of unsteady breaking waves in the absence of wind. Results focus on the air and water flow structure of representative spilling and plunging breaking waves.

1.2 Shoaling Wave Breaking

In experimental breaking wave studies, it is desirable for the waves to break in one repeatable location. In the present work, waves are forced to break via shoaling. The physical mechanism by which shoaling causes waves to break can be illustrated by examining the case of simple shoaling on a slowly varying bottom depth as presented in Svendsen [40]. The following derivation is essentially a condensed version of that presented in Svendsen [40] Chapter 3, and the reader is referred to that text for further detail. In this simplified case, the bottom is characterized by the shoaling parameter,

$$S = \frac{\lambda}{h}\frac{dh}{dx} \tag{1.1}$$

where λ is the wavelength, h is the bottom depth (which is a function of x) and $\frac{dh}{dx}$ is the slope of the bottom. Svendsen suggests that it is required that $S < 0.5$–1 for the assumption of a slowly varying bottom to be valid. In this case, the dispersion relation for linear waves on a constant bottom depth can be applied for any given x. The dispersion relation for linear waves is given by

$$\omega^2 = gk\tanh(kh) \tag{1.2}$$

where ω is the temporal frequency and $k = \frac{2\pi}{\lambda}$ is the wavenumber. It is also important to note that in this analysis the waves are monochromatic, and the frequency of the waves remains unchanged regardless of where the waves are on the shoal due to the conservation of wave crests.

If the width of the shoal is invariant, then the problem simplifies to the case Svendsen refers to as simple shoaling. The effect of the shoal on wave height can be examined by applying conservation of energy between two vertical sections at different x locations along the shoal, as shown in Figure 1-4 . If energy dissipation due to friction and breaking, and energy input due to wind is neglected, then the energy fluxed into the control volume at $S1$ must equal the energy flux out of the control volume at $S2$. Mathematically, the energy conservation reduces down to

$$H_1{}^2 C_{p_1}\left(1 + G_1\right) = H_2{}^2 C_{p_2}\left(1 + G_2\right) \tag{1.3}$$

where H is the wave height, C_P is the wave phase speed defined as

$$C_P \equiv \frac{\omega}{k} \tag{1.4}$$

and

$$G = \frac{2kh}{\sinh(2kh)} \tag{1.5}$$

Taking $S1$ to be in deep water and rearranging Equation 1.6, Svendsen presents a general ratio between wave height at any point along the shoal and the deep water wave height:

$$\frac{H}{H_0} = \left(\tanh(kh)\left(1 + G\right)\right)^{-1/2} \tag{1.6}$$

where H_0 is the wave height in deep water. When plotted, it is clear that wave height, H, increases with decreasing bottom depth (see Figure 3.5.6 in Svendsen).

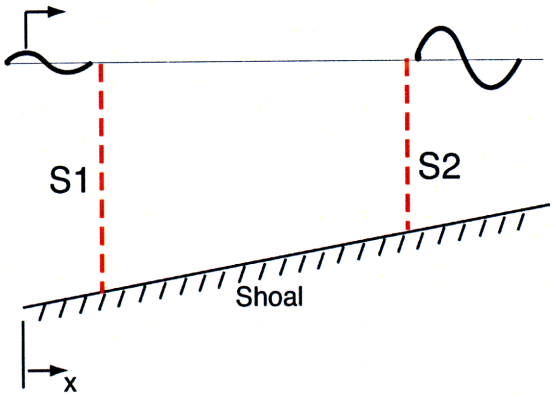

Figure 1-4: Control volume used for energy conservation along the shoal

Intuitively, as discussed by Svendsen, the physical mechanism for wave height increase is an increase in the local energy density. The wave height continues to increase until ultimately the wave breaks. Breaking dissipates energy and reduces the wave height.

1.3 Outline of Thesis

The remainder of this document is organized as follows. First, the experimental methodology is described in Chapter 2. This includes a discussion of the physical parameterization of breaking waves studied; which includes physical characteristics and non-dimensional numbers that describe the waves. Then, a thorough description of the wave measurement facility is provided, including discussion of the wave tank, wave generation and wave height gauges. As will become apparent, surface tension impacts the waves studied herein, and Section 2.3 describes the role of surface tension in wave breaking as well as the characterization of surface tension in this study. Section 2.4 delves into the details of the quantitative imaging technique. A general description of particle image velocimetry (PIV) is included, as well as seeding, illumination and imaging details from the present work. Finally, the data processing presented some unique challenges, and Section 2.5 discusses the treatment of raw data to extract useful results.

Results from the experiments and discussion thereof is the subject of Chapter 3. Particular attention is paid to the time evolution of velocity and vorticity for spilling

and plunging breakers studied. Conclusions from the study are drawn in Chapter 4. Also, some comparisons between the work presented herein and published work are made to put the study in a greater context. Appendix A includes details of a thorough PIV error analysis. Discussed in Appendix B are considerations for the difference in index of refraction between air and water, and how this affects imaging.

Chapter 2

Experimental Methods

The goal of this study was to develop a methodology for simultaneously measuring the water and air flow fields of breaking waves in the absence of wind, and to apply this method to several breaking waves to unveil flow physics. Several initial experiments on waves ranging from non–breaking to plunging breakers provided a test bed for the flow seeding, illumination and imaging methods. The results from these cases, some of which are presented Section 3, were used as feedback for the design of the measurement system. Then, the aim of the work turned to the investigation of flow physics using the developed method. Results from several of the preliminary experiments as well as experiments using the more developed method are presented in Section 3. The following section focuses on the wave measurement facility, surface tension, the flow seeding technique, quantitative imaging and data processing.

2.1 Physical Parameterization of Breaking Waves

Before diving deeper into the details of the experimental methods, the physical characteristics of the breaking waves studied are examined. Four cases of wave breaking were studied in the present work; each case involved a slightly different experimental setup for various reasons that will be elaborated on herein. The cases will be referred to by letter throughout this document. Cases A, C and D correspond to three different spilling breaking waves studied, and case B corresponds to a plunging breaking

wave. Certain physical attributes of the waves were measured in the pre-shoaling region by wave gauges and are summarized in Table 2.1. Section 2.2 provides details of the wave gauges and calculation of the physical attributes from gauge data. The physical parameters are not intended to relate breaking phenomena to pre-shoaling behavior; rather, the pre-shoaling characteristics provide some basis of comparison between the cases studied. In fact, the process of shoaling changed many of these parameters, as discussed in an earlier section. Nonetheless, the frequency, amplitude, phase speed and wavelength were measured and reported in Table 2.1. Also, several non-dimensional parameters characterized the waves upstream of the shoal. Using the wave phase speed, C_p, and wavelength, λ, as characteristic velocity and length scales, the Reynolds number, which relates inertial and viscous effects, is defined as

$$Re = \frac{C_p\ \lambda}{\nu} \tag{2.1}$$

where ν is the kinematic viscosity of the liquid phase. The Froude number, which relates inertial effects to gravitational effects, is defined as

$$Fr = \frac{C_p}{\sqrt{g\ \lambda}} \tag{2.2}$$

where g is gravity. The importance of inertia relative to surface tension is characterized by the Weber number, which is defined as

$$We = \frac{\rho\ C_p^2\ \lambda}{\sigma} \tag{2.3}$$

where σ is the surface tension at the liquid-air interface. The ratio of wave height to wavelength, $\frac{H}{\lambda}$, was calculated as well. Finally, the wave steepness is defined as kA where $k = \frac{2\pi}{\lambda}$ is the wavenumber and A is the amplitude.

In cases A, B and D, Isopropyl Alcohol (IPA) was added to distilled water to create the liquid phase of the flow. The reasons for adding IPA are discussed in section 2.3. For simplicity, the liquid phase will simply be referred to as water throughout this document; however, it is made clear what amounts on IPA were added to the water for each case. Viscosity for IPA/distilled water mixtures was calculated using the

Table 2.1: Pre-shoaling parameters for waves studied.

Case	A	B	C	D
Breaking Classification	Spilling	Plunging	Spilling	Spilling
$f\ (Hz)$	2	2	2	2
$A\ (mm)$	8.11	13.39	9.00	9.59
$C_p\ (cm/s)$	90.3	77.2	106.9	100.6
$\lambda\ (cm)$	45.2	38.6	53.4	50.3
$\frac{H}{\lambda}\ (cm)$	0.0359	0.0695	0.0337	0.0381
kA	0.1128	0.218	0.1059	0.1198
Re	3.85×10^5	2.81×10^5	5.70×10^5	4.93×10^5
Fr	0.429	0.397	0.467	0.453
We	8.56×10^3	5.34×10^3	9.91×10^3	9.75×10^3

empirical formula provided in Hirschfelder et al. [14],

$$log\eta = x_1 log\eta_1 + x_2 log\eta_2 \tag{2.4}$$

where x is the mole fraction of the particular component and η is the dynamic viscosity (equivalent to μ which is used more frequently in the fluid dynamics field), and the subscripts 1 and 2 refer to the individual components in the mixture. The density of the liquid mixture was calculated from

$$\rho = \frac{V_{IPA}}{V}\rho_{IPA} + \frac{V_{H_2O}}{V}\rho_{H_2O} \tag{2.5}$$

where V is the volume.

2.2 Wave Measurement Facility

The waves under investigation in this study were unsteady breaking waves generated by a paddle-type wavemaker and forced to break via a downstream shoal in a pre-existing small wave tank. A Solidworks model of the wave tank, as well as imaging

instrumentation is show in Figure 2-1. The inside dimensions of the acrylic wave tank measured 2.5 m in length, 16 cm in width and 18 cm in height. The resting fluid depth in the tank for the experiments presented herein ranged from 12.85–13 cm. Given that a main focus of this work involved measuring the air flow induced by wave breaking, it was necessary to enclose the tank as much as possible to mitigate the effects of ambient air currents. A tank enclosure constructed of thin acrylic sheets was attached to the existing tank, extending the height by 20 cm to an overall interior height of 38 cm and lidding the tank. The inside height of the enclosed tank was sufficiently large such that the air flow induced by breaking was not constricted in any way. An opening in the tank cover above the interrogation region allowed laser light to shine from above without attenuation. An opening was also placed in the downstream portion of the cover to allow for seeding of the air flow; a detailed discussion of the air flow seeding is provided in Section 2.4.1.

A hinged, acrylic, paddle type wavemaker generated a packet of waves of a single frequency which steepened and broke downstream due to the presence of an acrylic shoal . Wavemaker motion was provided by a SMAC linear actuator (model # LAS55-50-53-5) which has an encoder resolution of 5 μm and 0-5 cm programmable stroke amplitude. A pre-existing Galil motion control system provided closed-loop motion control for the actuator. The control system was composed of parts from Advanced Motion Controls including a Galil motion controller (DMC-1425) and interconnect module (ICM-1460), as well as a PWM servo amplifier (12A8) and power supply (PS2X300W). A Galil programming language was used to specify the motion of the actuator. An existing DOS command prompt was used to send stroke amplitude, frequency and cycles to the motion controller. This command prompt was incorporated into a LabView VI to simplify the overall interface with the hardware and instrumentation.

For the present study, all wavemaker motions were sinusoidal. Typically, five cycles of the motion were programmed, resulting in a packet of waves. The frequency of paddle motion could be varied from 0-4 Hz, though all waves studied herein were generated at a 2 Hz paddle frequency. The paddle amplitude could be adjusted to

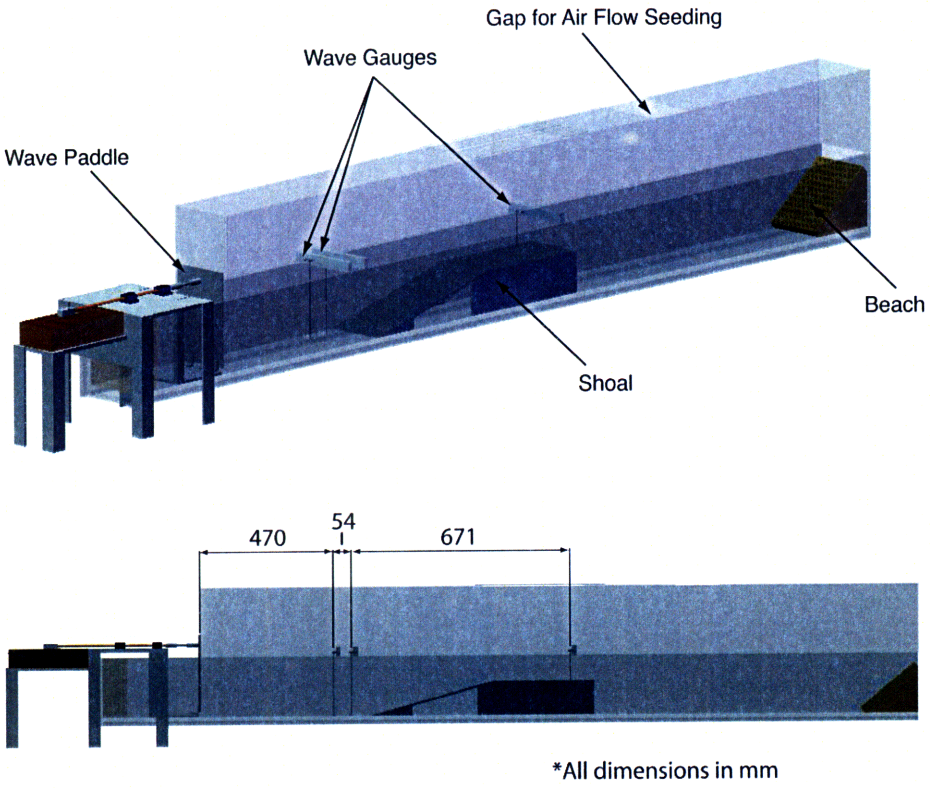

Figure 2-1: Solidworks model of the wave tank. Side view shows location of wave gauges in the tank.

generate non-breaking, spilling or plunging waves. The shoal, located 56 cm downstream of the wave paddle, caused the energy of the wave train to focus, and the height of the waves to increase until breaking occurred. The shoal consisted of a ramp with a 15° angle, and plateau with height 10.2 cm and length 30.6 cm. At the downstream end of the tank, a piece of reticulated, polyurethane foam mounted on an angled perforated plate diffused remaining wave energy to mitigate reflections from the end of the tank.

Three resistance style wave gauges modeled after a design described in Chen [6] were built into the tank to measure the wave height time records. As shown in Figure 2-1, two gauges were placed upstream of the shoal to measure pre–breaking wave heights, and one gauge was placed on the downstream portion of the shoal to measure the waves post–breaking. Sample wave height time records from all three

gauges are shown in Figure 2-2 for a representative spilling breaking wave.

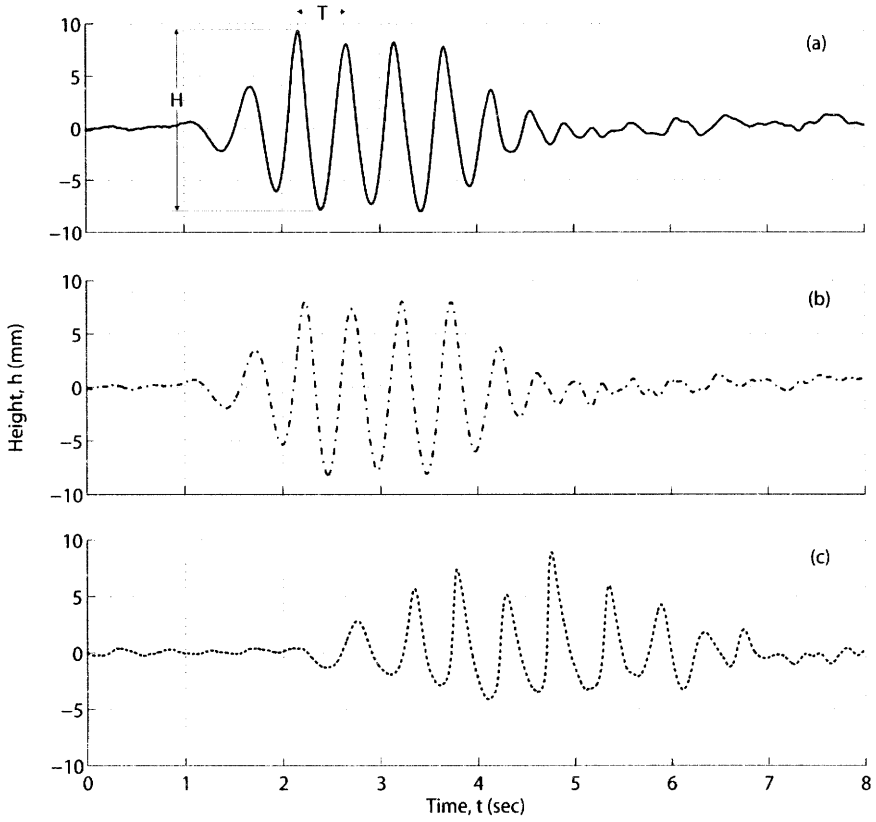

Figure 2-2: Sample wave gauge records from the two upstream wave gauges ((a) and (b)), and the downstream wave gauge (c).

The same circuitry described in Chen (1994) was used in the present study, but a slightly different gauge design was used. In order to ensure the gauges were minimally invasive to the flow, 1.6 mm diameter stainless steel wires were used as the leads for the gauges. The bottom of the leads were held in place by stainless steel set screws that threaded into a small acrylic block fixed to the tank bottom. Guitar pegs attached to an overhead mount held the top ends of the lead wires and allowed for easy adjustment of the tension. A reasonably high tension was applied to the leads such that the separation distance of 16 mm would not be altered by fluid forces. BNC cables with clamp-on connections attached the wave gauge leads to the measuring circuit. The output of the measuring circuit was sent to a National Instruments DAQ board which sampled the signal at a rate of 1000 Hz. Since the fluid used was a distilled water/IPA mixture, and the gauges measured conductance of the fluid, table

salt was added to make the fluid more conductive and thus increase the sensitivity of the gauges.

Upstream amplitudes for the breaking waves studied typically ranged from 8.1–13.4 mm, with smaller amplitudes generally corresponding to spilling breaking and larger amplitudes corresponding to plunging breaking for a fixed surface tension. The frequency of each wave train was easily calculated from a single wave gauge time record by dividing any number of crests in the packet by the time span between the crests. The wave phase speed was calculated by cross-correlating the wave records from the two upstream gauges to find the time shift, Δt, between wave records. Since the separation between the gauges, Δx, was known, the phase speed could be calculated from

$$C_p = \frac{\Delta x}{\Delta t} \tag{2.6}$$

This method assumes that the waves were of constant form (i.e. crests were not moving through the group and changing amplitude). It appears, from observation of the wave records in Figure 2-2 (a & b), that the probes were close enough to each other that the crests were in the same orientation relative to the group, and thus the assumption holds. In Figure 2-3(a) the trimmed time records from the first two gauges are plotted on on the same axes. In Figure 2-3(b), the record from the second gauge has been shifted by Δt corresponding to the shift causing the largest peak in the cross correlation.

If linear wave theory is employed, data from the upstream wave gauges could be used to calculate other pre-shoaling wave parameters, such as wavelength. Application of linear theory is valid when the wave height to wavelength ratio, $H/\lambda \ll 1$ (Svendsen [40]). The pre-shoaling values for $H/\lambda \ll 1$ for the wave cases studied herein are shown in Table 2.1; all values were much less than 1. Using the definition of the phase speed, the wavelength is calculated from

$$\lambda = \frac{C_p}{f} \tag{2.7}$$

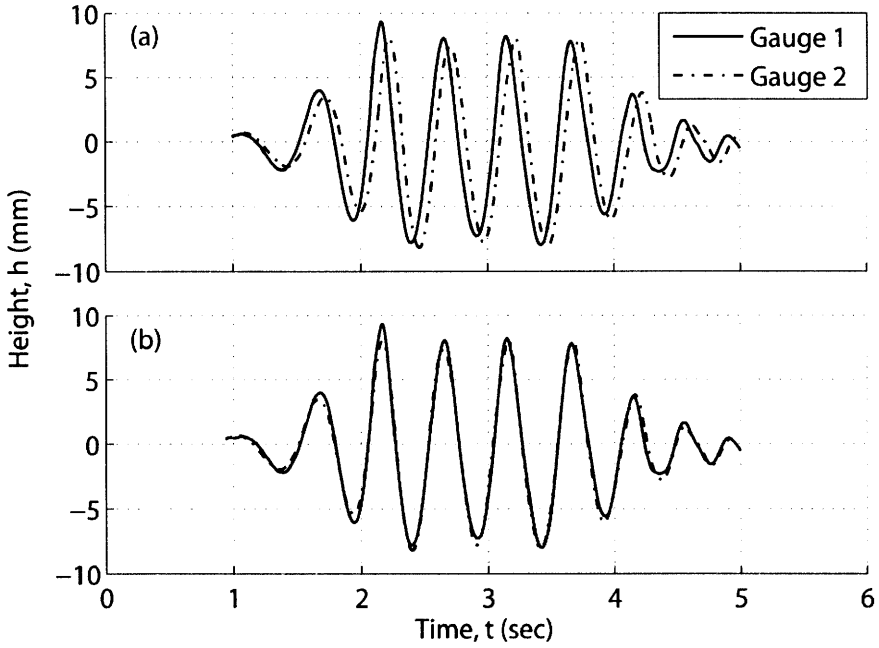

Figure 2-3: (a) Plot of wave records from upstream gauges. (b) Plot of wave records with the record from the second gauge shifted by Δt.

where f is the frequency of wave motion. Also of interest is the characterization of the pre-shoaling waves as deep water, shallow water or waves of intermediate depth. Deep and shallow water waves refer to situations where the dispersion relation, given in Equation 1.2, can be simplified. The deep water waves approximation is approached when kh becomes large enough such that $\tanh(kh) \rightarrow 1$, which essentially occurs when the ratio of bottom depth to wavelength, $h/\lambda > 1/2$ (Newman [29]). Shallow water waves, on the other hand, occur when kh becomes small enough such that $\tanh(kh) \approx kh$, which approximately occurs for $h/\lambda < 1/20$. For all waves studied in this work $1/20 < h/\lambda < 1/2$ in the pre-shoaling region, and thus are waves of intermediate depth in the pre–shoaling region.

2.3 Surface Tension

For certain scales of wave breaking, surface tension can affect the dynamics of the breaking process. In this study, the surface tension of the liquid was actually manip-

ulated to achieve desired breaking characteristics. This section discusses the general impact of surface tension on wave breaking as observed by other authors, as well as the measurement and manipulation of surface tension in the present work.

2.3.1 Effect of Surface Tension on Breaking Waves

At the length scales of the waves investigated in this study ($\lambda \approx$ 38–54 cm, $A \approx$ 0.8–1.4 cm), surface tension played an important role in the physics of wave breaking. Duncan [10] provided an extensive review of the effect of surface tension on wave breaking. Figure 2-4 is reprinted from Duncan's review article, and shows qualitatively the effect of surface tension on wave breaking. In Figure 2-4, each wave is still considered a spilling breaker even though a small jet appears in the wave with weak surface tension. Duncan pointed out that numerical studies of unsteady breakers have shown jet formation and impact (a signature phenomenon of plunging breakers) occurred whenever the wavelength was sufficiently long such that surface tension effects were negligible. In numerical studies, Tulin [41] found that surface tension starts impacting the physics of wave breaking for waves with wavelengths less than about 3 meters. For waves with wavelengths less than around 50 cm, Tulin noticed no jet formation, and the wave geometry was characteristic of spilling breakers. The upstream wavelengths of waves in the present study were all on the order of 50 cm, and shoaling actually causes the wavelength to decrease; therefore, surface tension was expected to play an important role in the physics of wave breaking. Ceniceros & Hou [4] used a numerical boundary integral method to study two-dimensional deep water breaking waves with surface tension effects. In their study, they varied the surface tension to examine the effect on the breaking wave structure. For zero surface tension, no capillary waves were observed and a jet formed. As surface tension was increased, capillary waves formed while the free surface still overturned, until a threshold surface tension value beyond which the surface did not overturn, and instead a bulge and capillary wave system appeared, as is typical in spilling breakers. Perlin et al. [32] experimentally studied a deep water plunging breaker dispersively generated with a wavelength of 80 cm at the center frequency. Using flow visualization, they observed

capillary waves on the front face of the wave even though a jet formed and impacted the free-surface, indicating that surface tension was not entirely negligible.

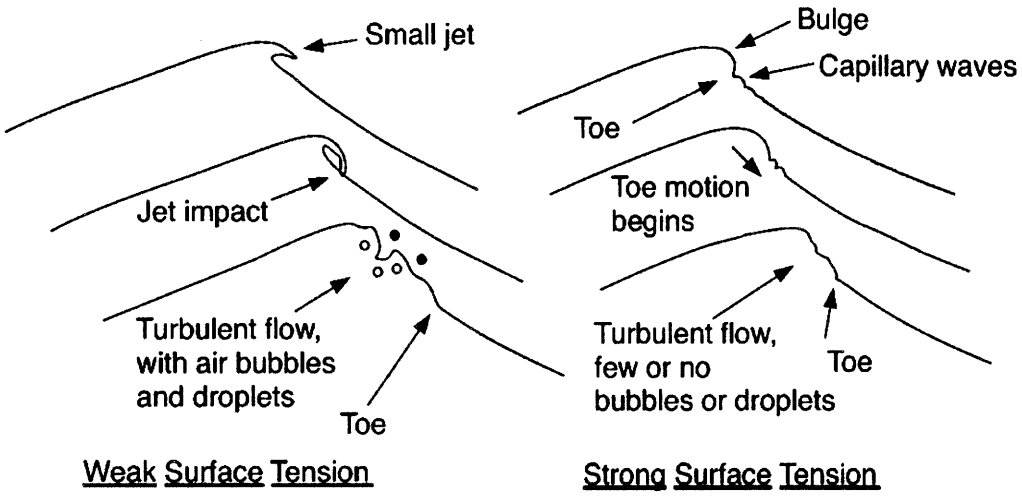

Figure 2-4: Qualitative effect of surface tension on wave breaking. (Reprinted from Duncan [10]

2.3.2 Measuring Surface Tension

The method adopted for measuring surface tension in the present study was the Wilhelmy plate technique, which characterizes static surface tension. A discussion of the theory of the Wilhelmy plate technique is provided in de Gennes et al. [9]. Figure 2-5 shows a schematic of the Wilhelmy plate measurement technique. Essentially, the purpose of the technique is to infer the surface tension by measuring the capillary force, which de Gennes et al. define as

$$F = p\sigma cos\theta \tag{2.8}$$

where σ is the surface tension, p is the perimeter of the contact line on the plate and θ is the angle of contact between the liquid and the plate. If the plate is very thin, the perimeter of the contact line is simply

$$p = 2L \tag{2.9}$$

where L is the length of the plate. The wetting angle θ is difficult to measure and brings an additional level of uncertainty to the measurement. However, as pointed out in de Gennes et al., if the plate material has a high surface energy it is possible to achieve a contact angle $\theta = 0$, and Equation 2.8 reduces to

$$F = 2L\sigma \tag{2.10}$$

Platinum is a typical material used for Wilhelmy plates, as it has a high surface energy and the surface can be regenerated by exposing it to a flame to keep it free from contaminants [9]. All that must be measured in this case is the length of the plate and the capillary force. In practice, a high precision balance is required to measure the capillary force. The balance registers an increase in mass which can multiplied by gravity to yield the capillary force. Thus, the surface tension can be found using

$$\sigma = \frac{mg}{2L} \tag{2.11}$$

Off-the-shelf surface tension measurement systems are typically designed as automated, self–contained units which measure an isolated sample. Since in this study it was important to measure surface tension *in situ*, the Wilhelmy plate method had to be adapted to the experimental facility. For guidance as to how to make Wilhelmy plate measurements in practice, advice was sought from KRÜSS [19], a company that manufactures surface tension measurement systems, including the platinum plate used in this study. A KRÜSS engineer advised that the measurement procedure implemented in their devices involves raising the sample into contact with the platinum plate. The height of the sample at initial contact is recorded. Then, the sample is raised to ensure proper wetting of the plate. Finally, the sample is lowered to the height of initial contact with the plate, and the force reading is taken.

For the measurements in this study, a thin platinum plate (length = 2 cm, height = 1 cm, thickness = 0.2 cm) was attached to a precision electronic balance (AND model HR–120). Obviously, when making *in situ* measurements, the sample could

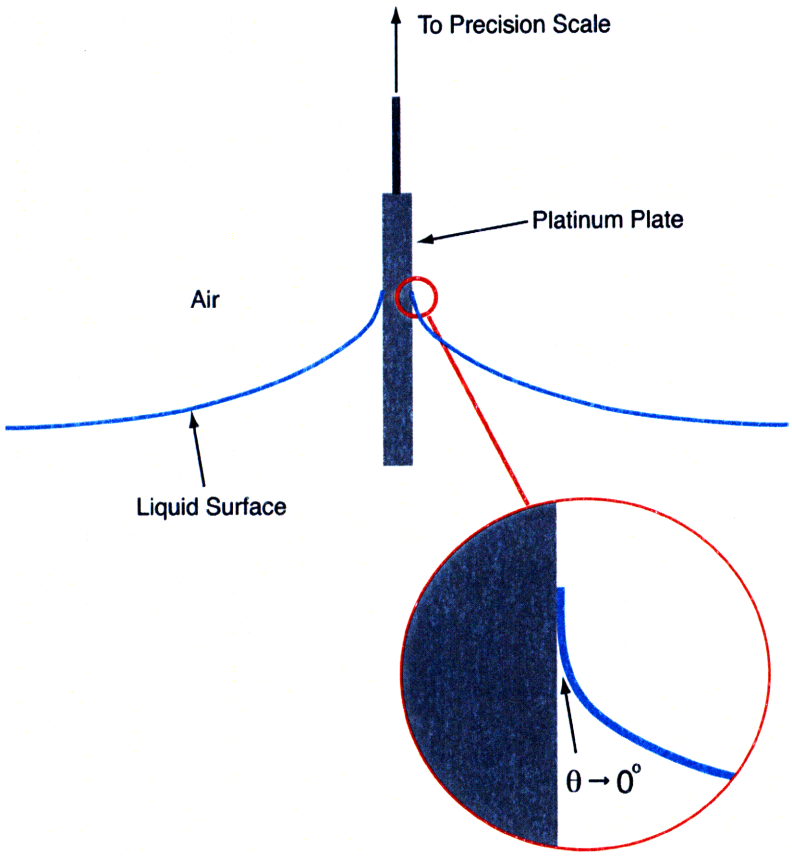

Figure 2-5: Schematic of Wilhelmy plate measurement technique.

not be raised and lowered very easily. In lieu of this, the plate was lowered about 0.7 cm into the liquid to ensure wetting, and slowly raised back up toward the height of initial contact with the liquid before taking the scale reading. At this point, surface tension forces held the fluid to the plate, and the increased force was detected by the balance. The mass reading on the scale was related to the surface tension using Equation 2.11. For experimental cases A & B, before each measurement the plate was cleaned with isopropyl alcohol (IPA), which was allowed to evaporate from the plate. Although in separate measurements of the surface tension of distilled water this plate cleaning procedure was used and results were consistent with published surface tension values, it is recognized that this is not the preferred cleaning procedure. As discussed in de Gennes et al. [9] and per conversations with a KRÜSS engineer [19], the appropriate method for surface cleaning and regeneration is to torch the plate. Therefore, this cleaning procedure was applied for experimental cases C & D. Before

each measurement, the platinum plate was rinsed with distilled water and then heated with a butane torch to renew the surface.

2.3.3 Surface Tension in the Present Study

Initial testing with distilled water (surface tension, $\sigma = 73$ mN/m) resulted in waves which were significantly influenced by surface tension for all paddle amplitudes and frequencies (see McDonald [25]). If the surface did overturn (in most cases it did not), the jet that formed was very small and not characteristic of a plunging breaking wave. Since a goal of this work was to investigate the air-water flow dynamics associated with spilling and plunging breaking waves, steps had to be taken to reduce the relative importance of surface tension. This was achieved by adding isopropyl alcohol (IPA, $\sigma = 22$ mN/m) to the distilled water resulting in a well-mixed fluid with reduced surface tension. IPA was chosen to reduce surface tension because it is miscible in water.

Figure 2-6 shows the surface tension of various concentrations of IPA in distilled water measured in isolated tests using the Wilhelmy plate method. Previous work (McDonald [25]) showed that the 10% IPA by volume solution allowed for the generation of repeatable spilling and plunging breaking waves. The measured static surface tension for this solution was 43 mN/m. With no IPA added to the distilled water, spilling breakers could still be formed.

In addition to the isolated surface tension measurements, *in situ* static surface tension measurements were made periodically throughout the course of a day of experimentation. These measurements are summarized in Figure 2-7. For cases A & B, the average static surface tension of the fluid was 42.6 mN/m with a standard deviation of 1.1 mN/m, corresponding to a 10% IPA solution. In case D, the average surface tension of 51.5 mN/m corresponded to a 5% IPA solution, and exhibited very little fluctuation throughout the experiment with a standard deviation of just 0.43 mN/m. The surface tension in case C displayed some strange behavior, and warrants further discussion. The fluid used for this case was pure distilled water, because plunging breakers were not of interest for the particular experiment. The published

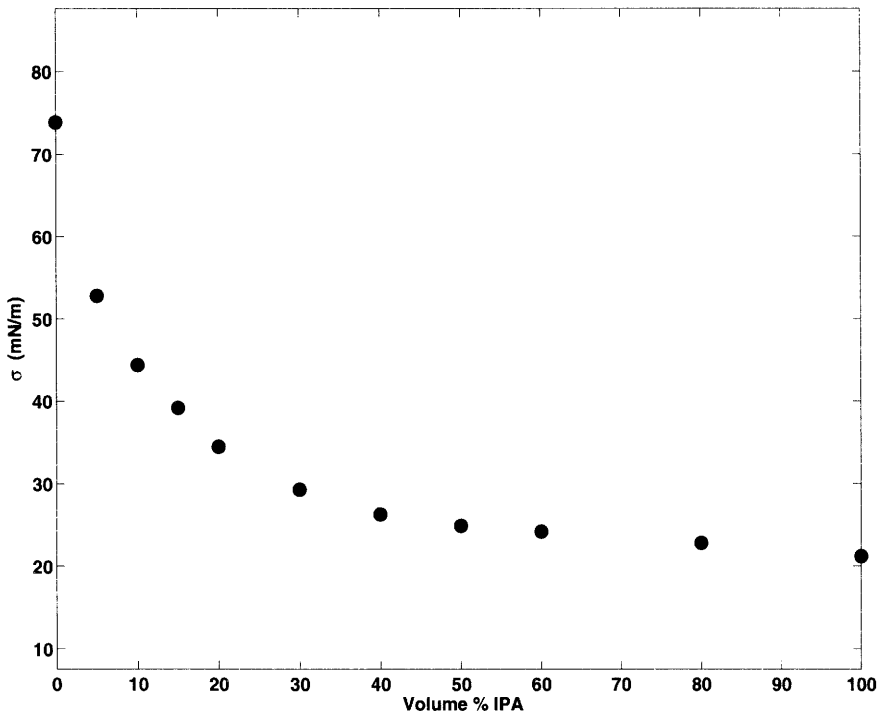

Figure 2-6: Surface tension vs. volume percent IPA. Measurements were performed using the Wilhelmy plate technique on isolated fluid samples.

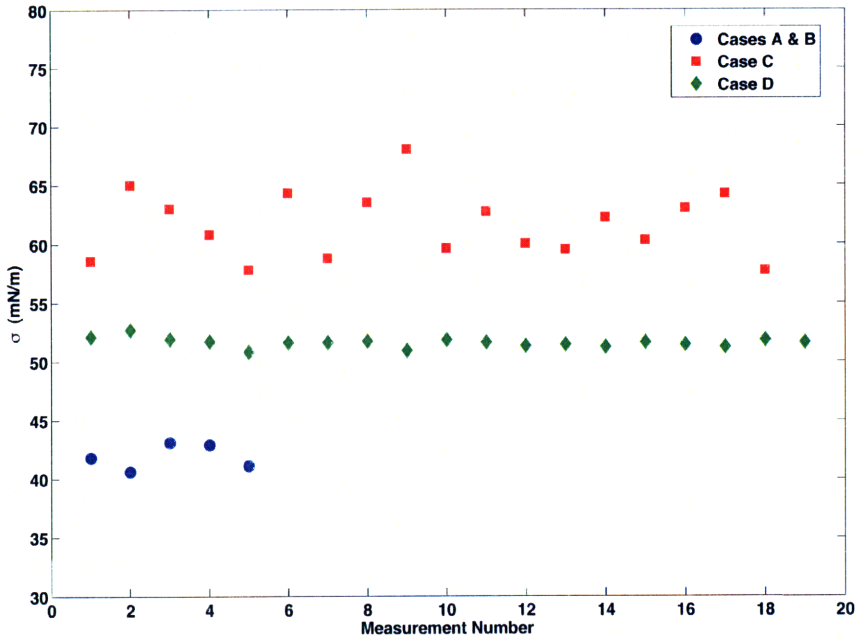

Figure 2-7: Surface tension throughout the experiments.

surface tension for pure distilled water is 73 mN/m, while the average measured surface tension for case C was 61.6 mN/m. In addition to the unusually low surface tension, the fluctuations were quite large, with a standard deviation of 2.82 mN/m. Some type of biological effect appeared to be at fault for the abnormal surface tension, which was apparently controlled when an IPA solution was used. Therefore, all experiments carried out since case C have made use of IPA in the liquid.

2.4 Quantitative Imaging

Particle Image Velocimetry (PIV) is the modern standard for quantitative imaging as it pertains to fluid mechanics. By far the most common measurement technique for resolving velocity fields is two-dimensional digital Particle Image Velocimetry (DPIV). Three-dimensional DPIV systems do exist, although most are still at the research level and are not readily available commercially. Two-dimensional DPIV is the main flow diagnostic used in the present work, and theory and implementation of this type of measurement is focused on herein.

The essence of PIV measurements involves using the motion of visible flow tracers (particles) to infer the velocity of the fluid. The schematic shown in Figure 2-8 provides an overview of the concepts of the PIV technique. The key assumption in the measurement, and a possible source of error, is that the motion of the flow tracers represents the motion of the fluid. Of course, this assumption is necessary to quantify the fluid velocity, because PIV is a visually-based measurement, and optical tracers must be placed in the fluid. Once seeded, illumination that provides high contrast between the flow tracers and the background is required. In two-dimensional PIV, only a planar cut of the fluid is measured; therefore, a laser sheet is often used as illumination. With present technology, digital cameras are the method of choice for image capture. In the study presented herein, high speed digital cameras enabled image capture at a rate of 500 frames per second (fps).

The captured digital images may or may not require pre-processing depending on the particular flow field in study. In the present work, extensive image pre-processing was required, and is thoroughly discussed in an ensuing section. In the next step of the measurement process, the pre-processed images are subjected to a statistical analysis to extract the velocity field. The theory behind the data acquisition and statistical analysis can be found in Willert & Gharib [45], Westerweel [43] and Raffel et al. [34]. The crux of the statistical analysis involves segmenting each image into windows (called interrogation windows) and performing a cross-correlation between windows of successive images in the time sequence. A peak in the cross-correlation

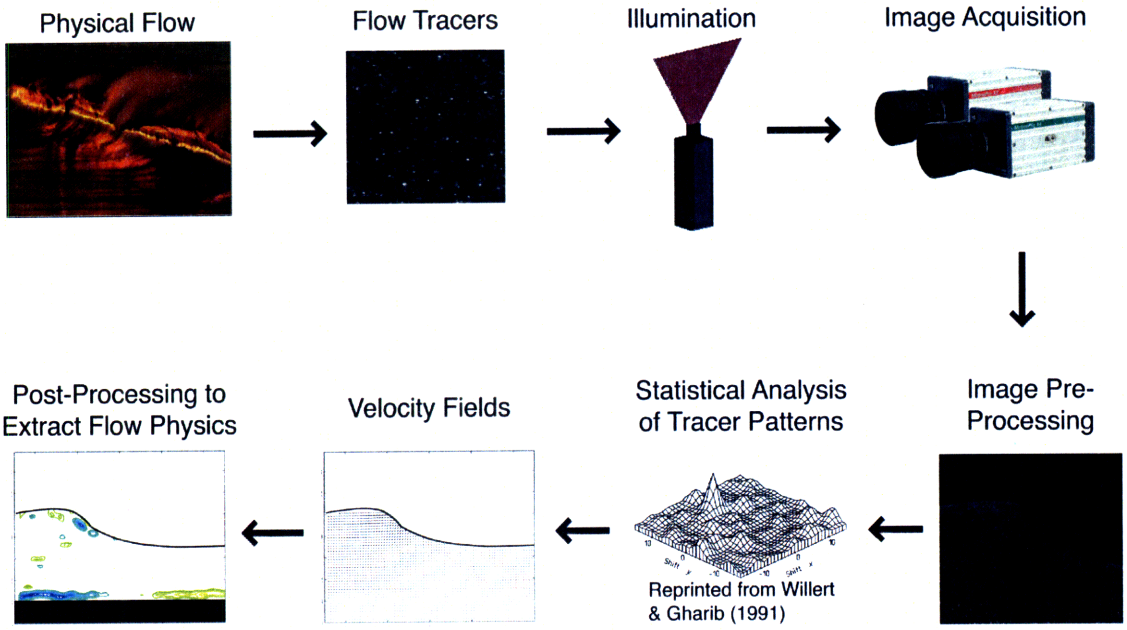

Figure 2-8: Flowchart illustrating the general concept of the PIV measurement technique.

corresponds to a statistically significant displacement of the tracer pattern within the interrogation window. The displacement corresponding to the largest peak in the cross-correlation is taken to be the displacement of the fluid within that interrogation window. With knowledge of the time between successive images, the velocity can be calculated. The processing is performed for each interrogation window and each pair of successive images, yielding a time series of velocity fields. Post-processing of the velocity fields provides insight into the flow physics.

The PIV technique has evolved for over two decades, and all the details and subtleties of the technique are not the subject of this thesis. For the purpose of this document, only details of the PIV technique relevant to the present work will be expounded upon. For more general and far-reaching information about PIV, the reader is referred to Adrian ([2],[1]) who offers reviews of early and of more modern PIV techniques. Also, Raffel et al. [34] provide a very useful PIV "handbook." For details on the error associated with PIV and analysis thereof, see Huang et al. [17], Westerweel [44] and Raffel et al. [34].

2.4.1 Flow Seeding

The flow tracers can be any one of a variety of solid or liquid materials, provided that they accurately track the flow and illuminate in the presence of a laser. An overview of seeding materials and characteristics is provided in [26].

Flow seeding in the water side of the flow for the present work was straightforward and traditional. For cases A, B and C, near neutrally buoyant hollow glass spheres (Potters Industries, Inc. Conduct-O-Fil) with mean diameter of 93 μm and density 1.1 g/cm^3 were used as optical flow tracers. For case D, Polyamid seeding particles (Dantec Dynamics, PSP–50) with a mean diameter of 50 μm were used. Due to the quiescent nature of the air flow (until the actual breaking event), seeding the air flow in these experiments presented a much greater challenge. Aside from appropriate size of the particles for PIV processing, the two functional requirements for the air flow seeding were:

1. Slow settling velocity compared to characteristic velocity of experiment.

2. Ability to track flow fluctuations.

Special emphasis had to be placed on appropriate size and low density of air flow seeding particles due to these requirements. Detailed analysis and comparison between seeding materials is discussed below.

Prior breaking wave experiments aimed at capturing the air flow have been performed in the presence of wind. Such experiments made use of air flow seeding similar to that found in traditional wind tunnel experiments (e.g. [36], [42], [18]). Small liquid or solid particles were generated via atomizers or aerosol seeders and injected into the mean flow. For experiments with ambient wind, the ability of the particles to track flow fluctuations (functional requirement 2) is of critical importance, yet the settling characteristics of the particles (functional requirement 1) are of less importance since the mean velocity (wind speed) is usually much larger than the gravitationally induced particle settling velocity.

In the present study, the air flow is quiescent until the breaking wave event. In the absence of wind, the settling velocity of the particles becomes as important a

Table 2.2: Comparison of physical characteristics of various air flow seeding materials

Seeding Material	Expancel® Microsphere	Paraffin Oil Droplet	Water Droplet	Glass	TiO_2
$d_p\,(\mu m)$	25	25	25	25	25
$\rho_p\,(kg/m^3)$	70	860	1000	2600	3500
$U_g\,(mm/s)$	1.27	15.81	18.39	47.85	64.42
$\frac{U_g}{C_p}\,(\%)$	0.165	2.05	2.38	6.20	8.34
Re	0.002	0.025	0.029	0.077	0.103
$N_{s,crit}$	5.68	17.84	19.19	30.42	35.26
$f_{s,crit}\,(Hz)$	123.3	12.5	10.8	4.3	3.2

consideration as the flow tracking capabilities. Thus, functional requirement 1 had to receive as much attention as functional requirement 2 when selecting particles. For spherical particles, Raffel et al. [34] have used Stokes drag law as a theoretical estimate of the gravitationally induced settling velocity. Stokes drag law is defined as

$$U_g = {d_p}^2 \frac{\rho_p - \rho}{18\mu} g \tag{2.12}$$

where d_p is the particle diameter, ρ_p is the particle density, ρ is the fluid density, μ is the fluid dynamic viscosity, and g is gravity. Table 2.2 shows a comparison of settling velocities for various seeding materials of appropriate size for the present experiment (particle diameter $\approx$ 25 μm). The theoretical particle settling velocities are also tabulated as a percentage of the smallest wave phase speed measured by the upstream wave gauges, in order to compare the settling velocity with a characteristic velocity of the experiment. This phase speed was 77.2 cm/s and corresponded to the plunging breaker in case B. Obviously, the Expancel® Microspheres possessed the most desirable theoretical settling characteristics.

The second functional requirement of the particles was the ability to track turbulent flow fluctuations. The analysis used here was based on a description of dynamic behavior of particles in turbulent flow presented in Hjelmfelt & Mockros [15], who provide a relationship between a particle to fluid velocity ratio, defined as

$$\eta = \frac{V_p}{V_f} \tag{2.13}$$

and the Stokes number, which is defined as

$$N_s = \sqrt{\frac{\nu}{\omega {d_p}^2}} \tag{2.14}$$

where ω is the radial frequency of velocity fluctuation, ν is the fluid kinematic viscosity and d_P is the particle diameter. The relationship is parameterized by the particle to fluid density ratio,

$$s = \frac{\rho_p}{\rho} \tag{2.15}$$

In addition to the "general" solution presented in Hjelmfelt & Mockros, they also present several approximations that simplify the solution. However, in this study we use the general solution to predict and compare the turbulent tracking capabilities of various seeding particles. Melling [26] investigated the suitability of several materials as flow tracers for PIV using the "Type III" approximation presented in Hjelmfelt & Mockros, defining as a design criterion for suitable flow tracking an amplitude ratio of $\eta = 0.99$. The same amplitude ratio was applied as the design criterion for the particles used in this work. Figure 2-9 shows a plot of amplitude ratio versus Stokes number for several particle density ratios which correspond to the particle materials under consideration for this study. By finding the Stokes number corresponding to $\eta = 0.99$ for a given material, one can then evaluate the maximum turbulent frequency that can be tracked. Table 2.2 shows the maximum turbulent frequency that particles of various materials can track using the amplitude ratio criterion of $\eta = 0.99$. The Expancel® Microspheres outperformed other materials in this regard as well, and were thus chosen as flow tracers for the present work.

In addition to the theoretical capabilities of the Expancel® Microspheres, Sankar et al. [37] have shown these particles outperform the traditional water droplets used in wind tunnel experiments. The authors show that the Microspheres demonstrate superior dynamic response across a range of particle sizes, as well as improved accuracy

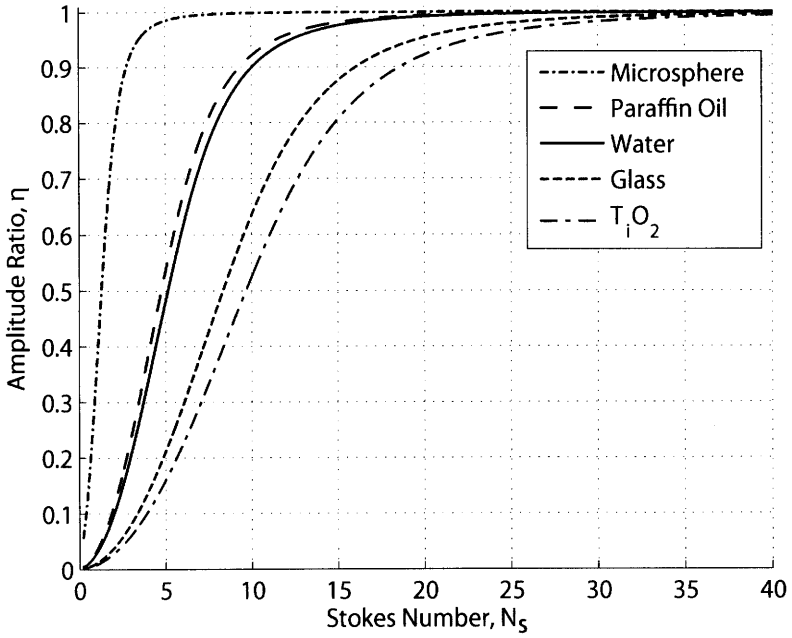

Figure 2-9: Amplitude ratio (η) vs. Stokes number (N_s) for various density ratios evaluated using the work of Hjelmfelt & Mockros [15]

in measuring the flow of a canonical circular cylinder experiment.

In the present work, the air seeding particles were introduced into the flow downstream of the shoal using a large pipette to lightly puff the particles near the region of interest. Any transient motion of the particles quickly dissipated, and the particles slowly sunk toward the free-surface. In order to better quantify the actual settling characteristics of the Expancel® Microspheres *in situ*, PIV data for times after introducing the particles into the region of interest, but before motion of the free-surface due to the wave packet began were analyzed. Data was averaged from many different experiments, and it was found that the magnitude of the average vertical settling velocity was 1.12 cm/s with a standard deviation of 1.24 cm/s, which were 1.45% and 1.61% of the wave phase speed of the plunging breaker in case B (77.2 cm/s).

2.4.2 Illumination

To simultaneously investigate the liquid and air flow induced by the breaking wave event, two near infrared (IR) lasers provided illumination for the flow, as shown

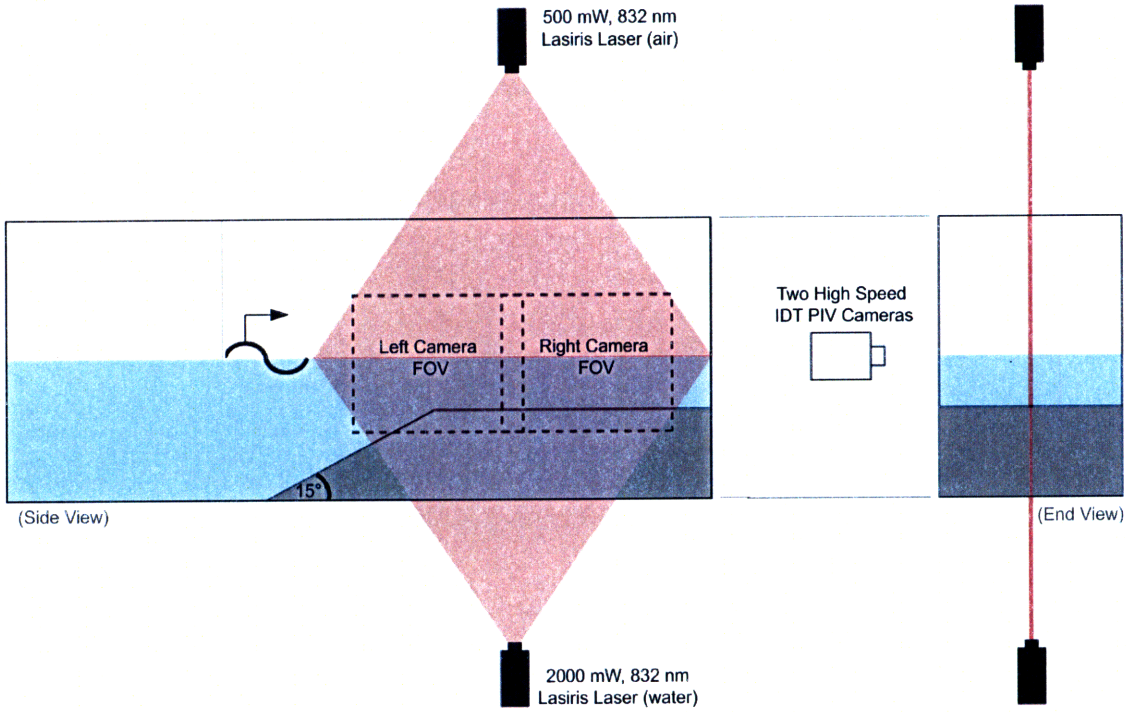

Figure 2-10: Schematic of the dual laser, side–by–side camera PIV setup. (Not drawn to scale).

in Figure 2-10. Preliminary studies showed that the use of one laser, shining from either above or below, created a non-uniform intensity profile in the opposite medium which varied as the wave passed; this would corrupt the PIV processing resulting in unreliable data. Using two lasers created a far more uniform light intensity profile in the air and liquid. A 2000 mW, 810 nm wavelength Lasiris™ Magnum II laser diode line generator with a fan angle of 15° mounted underneath the wave tank illuminated the liquid side of the flow. A 500 mW, 810 nm wavelength Lasiris™ Magnum II laser diode line generator with a fan angle of 10° was mounted above the tank to illuminate the air flow. According to the specifications provided by hte laser manufacturer, it is estimated that the thickness of the laser sheets in the region of interest was approximately 0.4 mm. Careful laser alignment ensured coplanarity of the laser sheets.

2.4.3 Imaging

High speed digital cameras capable of 1 kHz frame rates or higher have become more affordable in recent years. Using this type of camera, it is possible to achieve fully time-resolved PIV data. With the lasers operating in continuous mode, the possibility of over-exposure of the camera exists. Since the particles are moving with some velocity, it is possible that particle images may move appreciably (several pixels) if the camera exposure time is too long. The camera exposure time should be long enough to provide good contrast between the particles and the background, but short enough so that the particles don't streak. High speed cameras framing at 500 frames per second (fps) used in several configurations enabled fully time-resolved capture of the flow fields for the breaking waves studied herein.

Experimental cases A & B were carried out using two side-by-side, horizontally mounted (0° tilt angle) synced CCD cameras. A schematic of this camera setup is shown in Figure 2-10. The two side-by-side camera setup enabled measurement of both plunging and spilling waves - which broke at different locations along the shoal - with sufficient resolution using a single PIV setup. The camera fields of view were slightly overlapped along the direction of wave propagation. Because the index of refraction of water is larger than that of air, and since the numerical aperture (NA) of each camera was fixed, the angular acceptance of light rays emanating from the object plane was larger for the air than for the water. In other words, considering the air and water portions of the image separately, the effective field of view (FOV) was slightly larger in the air than in the water; thus, the calibration (pixels/cm) was smaller for the air. For an extended discussion of this effect, see Appendix B. However, since the distance from the object plane to the tank wall was small, the calibrations for air and water were very close, and a single calibration was applied to the entire image in post–processing. The left camera was an X-Stream Vision XS-3 high speed CCD camera (1260 x 1024 pixels) with an 85 mm lens. The camera calibrations were about 106 pixels/cm for the water portion of the images and 103 pixels/cm for the air portion. The right camera was a Motion Pro X3 high speed

CCD camera (1280 x 1024) with a 105 mm lens. Camera calibrations for the right camera match those of the left camera to within 1 pixel/cm. The fields of view of the cameras overlapped by about 50 pixels in the direction of wave propagation. Each camera acquired 8-bit images at a rate of 500 frames per second (fps) with a 1997 μsec exposure time. Figure 2-11 shows a raw image of the spilling breaking wave studied in case A. The particles in each medium were reasonably well in focus, as expected given the similar effective FOV for each medium.

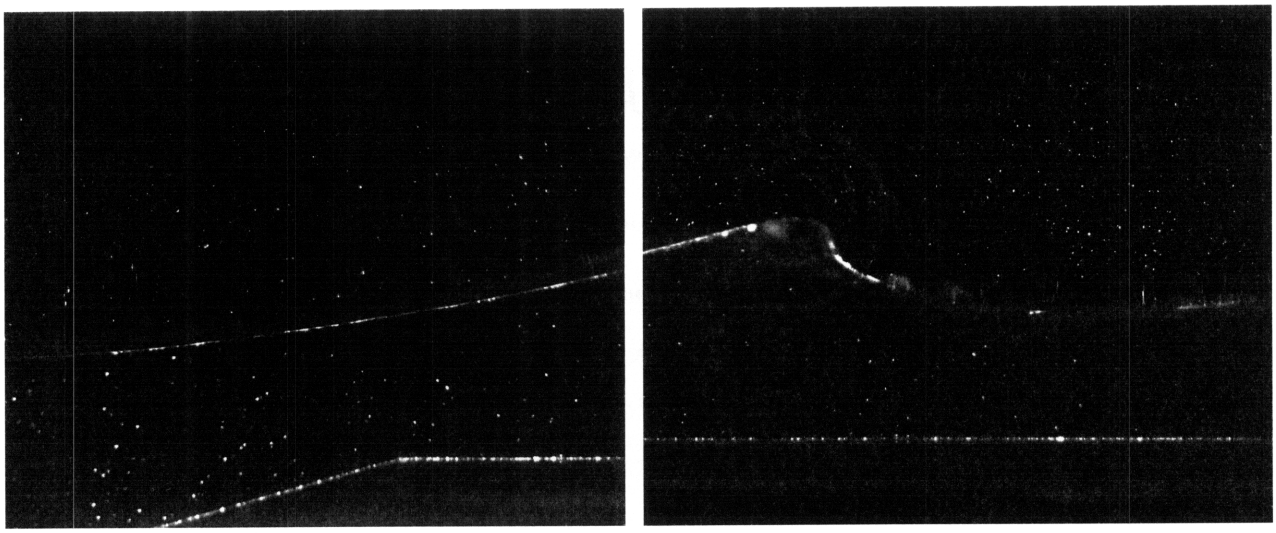

Figure 2-11: Sample raw images from the side–by–side camera setup. Images are from the spilling breaker in case A.

Further investigation of the raw images in Figure 2-11 revealed some streakiness near the surface, particularly in the right image. The meniscus formed by the water on the near tank wall actually caused this streakiness, and it appeared in the images because the camera image plane was coplanar with the laser plane (i.e., camera was not angled). Therefore, the wall meniscus partially masked the line of sight of the camera to some near surface particles. Figure 2-12 shows the raw image from the right camera with the free-surface and streaking due to the meniscus labeled. The desire to capture reliable near-surface data necessitated a method of image capture that avoided this masking. This issue of masking in breaking waves PIV studies was discussed by Melville et al. [28], and their solution was to angle the camera to cause

the actual free surface and the near-wall meniscus to appear at distinct locations in the image. For experimental cases C & D, one camera looking down at the surface from above captured the air side flow field, while a second camera looking up at the surface captured the water flow field, as shown in the schematic in Figure 2-13. For case C, the respective angles were $\alpha = 3.7\ ^\circ$ and $\beta = 3.5\ ^\circ$, and for case D the angles were $\alpha = 4.5\ ^\circ$ and $\beta = 5.5\ ^\circ$. Figure 2-13 also shows that the light rays coming from the near wall meniscus and the intersection of the laser light sheet with the surface enter the cameras at different angles with respect to the optical axis, and thus appear at distinct locations on the image plane. The camera and lens used to image the air in cases C & D was the same as the left camera for cases A & B, and the camera and lens used to image the water was the same as the right camera.

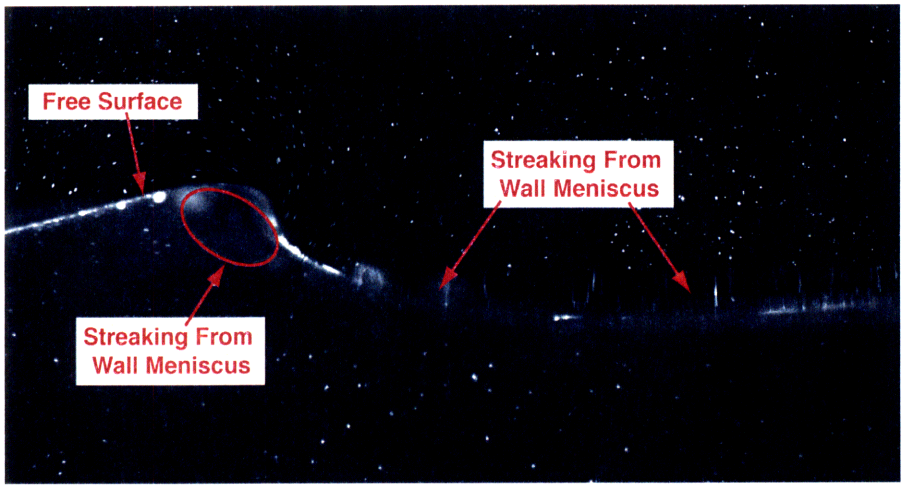

Figure 2-12: Image from the right camera of the side–by–side camera setup with free surface and meniscus streaking labeled. Image is from the spilling breaker in case A

Figure 2-14 show sample raw images for the same timestep from the air and water cameras for the spilling breaker in case C. Clearly, the meniscus no longer obstructed the surface and near-surface particles, enabling velocity measurements much closer to the surface. Figure 2-15 shows a zoomed view of the raw image from the water camera with the free-surface and near wall meniscus labeled. By virtue of the camera setup, the water camera FOV was smaller than the air camera FOV, making processing of the data somewhat less convenient than the side-by-side camera setup.

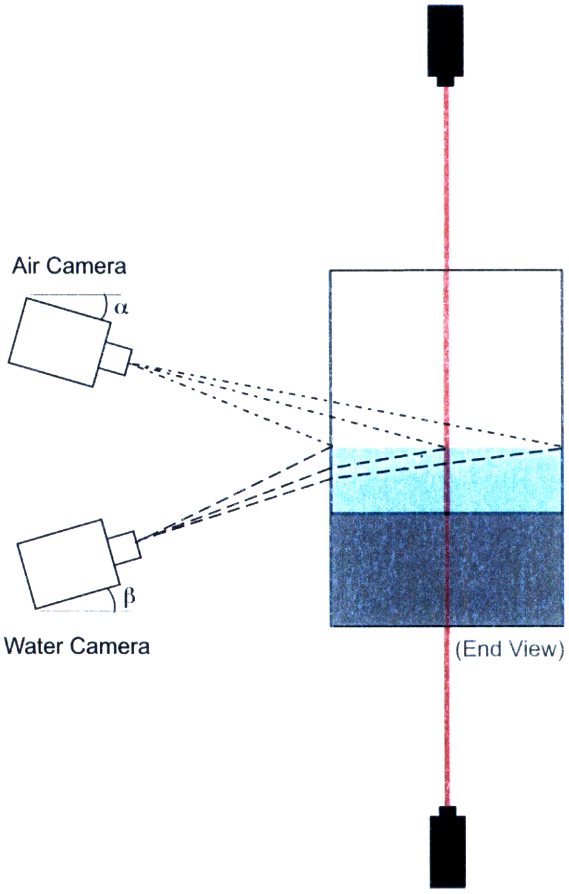

Figure 2-13: Schematic of the angled camera setup PIV setup. (Not drawn to scale).

2.5 Data Processing

For all experimental cases presented herein, some level of image pre-processing was performed. Since experimental cases A & B were used as a proof-of-concept, less image pre-processing was applied to these cases, because the results guided the image acquisition and processing in ensuing cases. Focus will first be given to the details of the images and pre-processing for cases A & B. Although some of the near-surface data from cases A & B proved unreliable due to the meniscus masking, use was still made of the data sets to gain insight into large scale features of the flow, to prove the validity of the flow seeding method, and to guide future experiments to be able to capture the relevant phenomena. Image pre-processing consisted of a non-linear subtract sliding minimum filter to remove constant image noise and smooth the original image which was implemented in the LaVision commercial software package

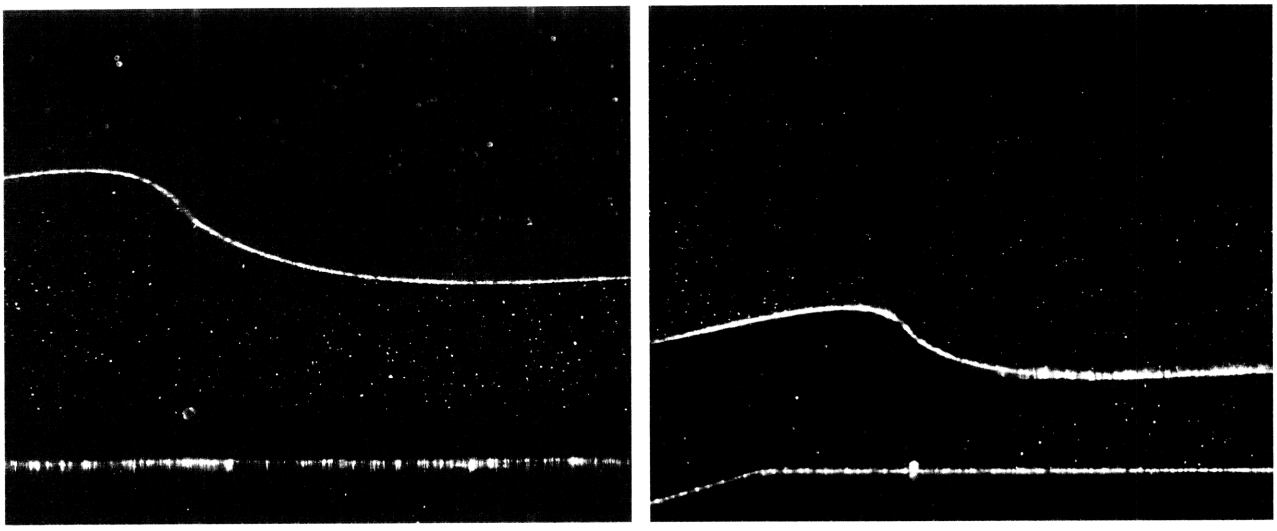

Figure 2-14: Sample raw water image (left) and air image (right) from the angled camera setup. Images are from the spilling breaker in case C.

DaVis 7.2.

For experimental cases C & D, each camera corresponded to a separate medium and the images from each camera were treated as separate data sets for processing. The portion of the image consumed by the opposite medium was not of interest, and would in fact introduce error into the PIV processing if not segmented from the image. Additionally, the bright surface would introduce false phenomena if left in the image for PIV processing. Other authors who have performed free-surface PIV experiments also discuss the need to remove the surface for PIV processing; see, for example, Dabiri & Gharib [8] and Melville et al. [28]. The images were thus preprocessed to segment the air and water for PIV processing. First, the location of the surface in each image was defined by hand-selecting a series of points from the raw images, then using cubic splines to interpolate between the points and extrapolate beyond the end points. Two such curves were defined for each image: a curve that defined the perceived location of the geometric free-surface, and a curve used to segment the medium of interest from the bright free-surface and the opposite medium. The former curve simply provided information about the orientation of the surface throughout the breaking process and was not used in the image pre-processing. Figure 2-16 shows

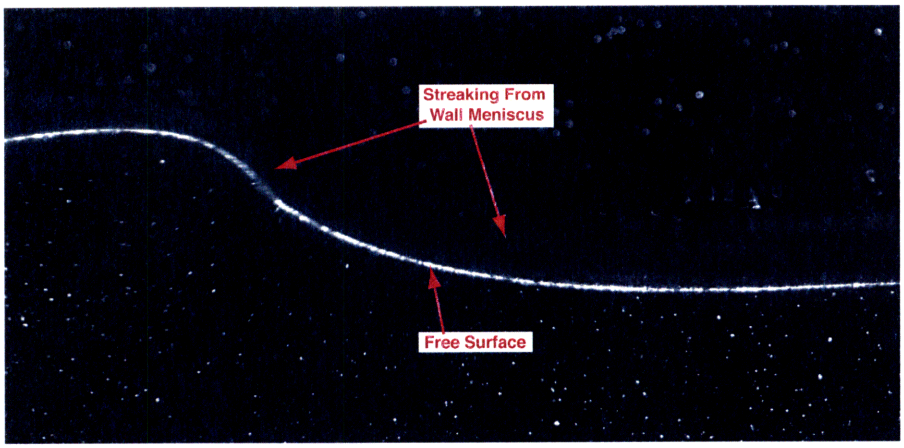

Figure 2-15: Image from the water camera of the angled camera setup with free surface and meniscus streaking labeled. Image is from the spilling breaker in case C.

a raw image from the water camera with both surfaces overplotted. A zero intensity value was assigned to all pixels above the masking surface for the water images and all pixels below the masking surface for the air images. The result was a set of "masked" images, with only particles of the medium of interest showing. Figure 2-17 shows the water image from Figure 2-14 after the masking process. The masking process ensured that only pixels in the medium of interest contributed to the PIV processing.

Due to the collection of a small amount of the Expancel ® Microspheres on the surface, the pixels just above the surface in the air images were very bright. An additional pre-processing routine on the air images reduced the effect of these high intensity pixels, which may have introduced error into the PIV processing. Before performing the masking routine, low frequency image content was removed using a two-dimensional high-pass spatial filter in MatLab. The filter retained high frequency image content, such as the seeding particles, but removed most of the free-surface, which was low frequency content. The image intensity was rescaled to emphasize brighter content that was retained, and then the image was masked. Figure 2-18 shows a raw air image with the bright surface side-by-side with the filtered, intensity adjusted and masked image. The filter did introduce an artifact near the edge of the surface where the pixels transitioned from bright to dark, which was a high frequency component of the image. For air the images in case C, this artifact of

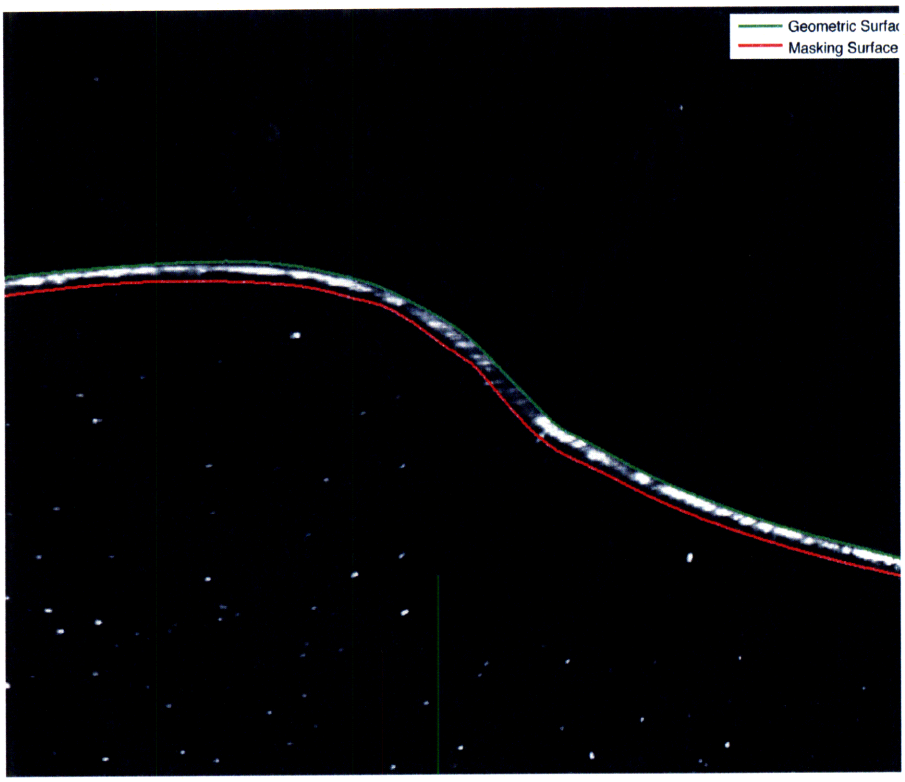

Figure 2-16: Image from the water camera of the angled camera setup with geometric and masking surfaces plotted. Image is from the spilling breaker in case C.

the pre-processing remained in the images. For the air images in case D, this was compensated for by masking the artifact at the edge by placing the masking surface a few pixels further into the air medium.

Actual PIV processing to calculate velocity fields was performed using the LaVision commercial software package DaVis 7.2. Tables 2.3 through 2.5 summarize the essential information about the PIV processing, including resolution and error, for each experimental case. Details of the error analysis for which results are presented in the aforementioned tables can be found in Appendix A. The tables include the camera calibrations, K, applied to the fields, as well as PIV interrogation window size and overlap. Also included is the spatial resolution of the velocity measurements in physical units, and the error thereof. Finally, error on the velocity and vorticity measurements are included. The error analysis presented in Appendix A shows that the error on velocity is a function of the magnitude of velocity. In the tables, error for input velocities of 4, 8 and 16 pixels/frame are shown, to give a sense of the error

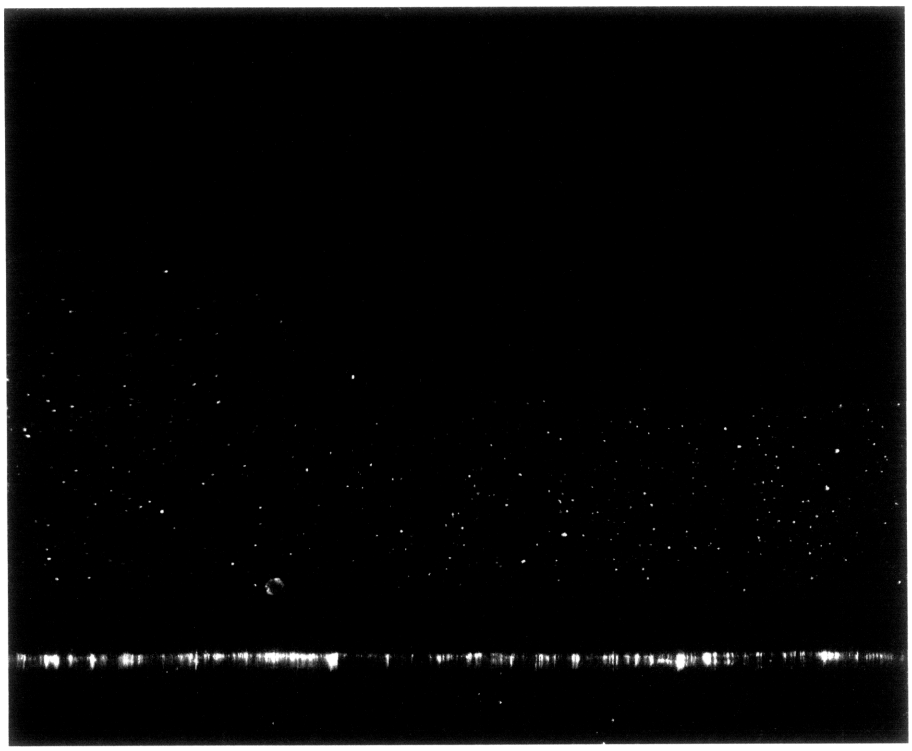

Figure 2-17: Sample masked water image from the angled camera setup. Image is from the spilling breaker in case C.

on typical values of velocity.

For cases A & B, image pairs of interest were processed using a multi-pass time-series cross-correlation resulting in a final window sizes of 32 x 32 pixels with 50% overlap. A median filter was applied to remove spurious vectors that varied from some threshold of neighboring vectors. Finally, an interpolation routine filled any empty locations in the vector field.

The water images in cases C & D were first pre-processed in DaVis 7.2 using the non-linear subtract sliding minimum filter. The same multi-pass time-series cross-correlation with final window sizes of 32 x 32 pixels with 50% used for cases A & B was used to calculate the vector fields for the air and the water in cases C & D. The masked region of the images produced no vectors. A median filter removed spurious vectors, and subsequently one of two operations smoothed the vector field. For the water fields in case C and the air fields in cases C & D, a non-linear denoising and robust smoothing filter was applied, which replaced each vector with a vector

Table 2.3: Summary of PIV resolution and error for case A.

Camera		Air Left	Air Right	Water Left	Water Right
Camera Calibration, K *(pix/cm)*		104.4	104.8	104.4	104.8
PIV Interrogation Window Size *(pix)*		32 × 32	32 × 32	32 × 32	32 × 32
PIV Interrogation Window Overlap *(%)*		50	50	50	50
Spatial Resolution *(cm)*		0.1533	0.1526	0.1533	0.1526
e_K (cm)		1.600	1.433	1.600	1.467
e_{res} (cm)		0.0024	0.0021	0.0023	0.0021
$e_{U_{PIV}}$ $(pix/frame)$		0.1	0.1	0.1	0.1
e_U (cm/s)	$U_{PIV} = 4$ $(pix/frame)$	0.573	0.553	0.551	0.537
	$U_{PIV} = 8$ $(pix/frame)$	0.777	0.722	0.740	0.701
	$U_{PIV} = 16$ $(pix/frame)$	1.305	1.176	1.233	1.140
e_{ω_z} (s^{-1})		1.9063	1.9063	1.9063	1.9063

Table 2.4: Summary of PIV resolution and error for case B.

Camera		Air Left	Air Right	Water Left	Water Right
Camera Calibration, K *(pix/cm)*		104.7	105.6	104.7	105.6
PIV Interrogation Window Size *(pix)*		32 × 32	32 × 32	32 × 32	32 × 32
PIV Interrogation Window Overlap *(%)*		50	50	50	50
Spatial Resolution *(cm)*		0.1529	0.1515	0.1529	0.1515
e_K (cm)		1.075	0.883	1.025	0.917
e_{res} (cm)		0.0016	0.0013	0.0015	0.0013
$e_{U_{PIV}}$ $(pix/frame)$		0.1	0.1	0.1	0.1
e_U (cm/s)	$U_{PIV} = 4$ $(pix/frame)$	0.523	0.504	0.507	0.497
	$U_{PIV} = 8$ $(pix/frame)$	0.627	0.576	0.599	0.570
	$U_{PIV} = 16$ $(pix/frame)$	0.936	0.802	0.873	0.799
e_{ω_z} (s^{-1})		1.9063	1.9063	1.9063	1.9063

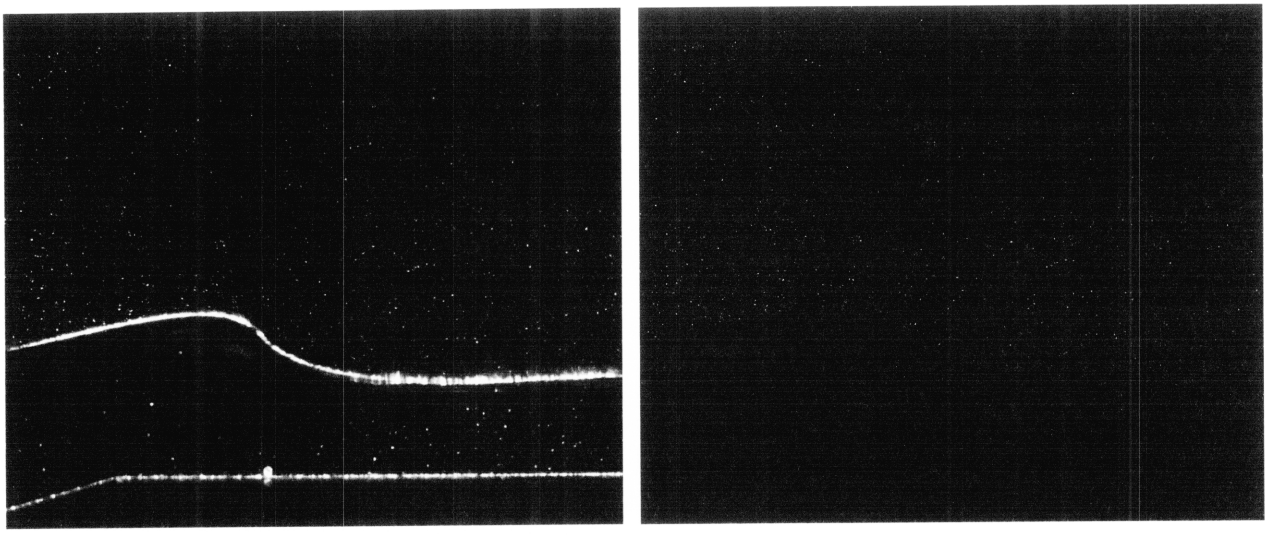

Figure 2-18: Raw air image (left) and filtered, adjusted and masked air image (right). Images are from the spilling breaker in case C.

calculated from a second order polynomial fit to neighboring vectors. One pass of a 3×3 smoothing filter was applied to the water vector fields for case D. Again, an interpolation routine filled any empty vector locations. Any remaining spurious vectors were removed by hand and replaced with the average of the nearest valid neighboring vectors. Based on an analysis of PIV algorithms presented in Stanislas et al. [39], it was estimated that the rms uncertainty on the velocities due to the PIV algorithm used for all cases herein was 0.1 pix/frame.

As mentioned earlier, the perceived actual free-surface was defined by hand-selecting a series of points and interpolating between the points with cubic splines; this surface was used solely for plotting and examination of the orientation of the surface throughout the breaking process. Velocity fields output from DaVis had units of pixels/frame, and needed to be calibrated to have physical units. The camera calibration coefficient converted pixels to the desired physical dimension (cm in this case), and the frame rate dictated the time spacing between frames (500 fps). Due to the difference in index of refraction for air and water, the camera calibration, K, was different for each respective medium for cases A & B. However, since these cases were used as an initial investigation into the problem, and since the calibrations were

Table 2.5: Summary of PIV resolution and error for cases C & D.

Camera		Air Case C	Water Case C	Air Case D	Water Case D
Camera Calibration, K *(pix/cm)*		75.9	126.7	77.5	118.2
PIV Interrogation Window Size *(pix)*		32 × 32	32 × 32	32 × 32	32 × 32
PIV Interrogation Window Overlap *(%)*		50	50	50	50
Spatial Resolution *(cm)*		0.211	0.1263	0.207	0.1354
e_K (cm)		3.2e-4	1.71e-4	3.1e-4	1.84e-4
e_{res} (cm)		8.9e-7	1.7e-7	8.25e-7	2.11e-7
$e_{U_{PIV}}$ $(pix/frame)$		0.1	0.1	0.1	0.1
e_U (cm/s)	$U_{PIV} = 4$ $(pix/frame)$	0.6588	0.3946	0.6452	0.423
	$U_{PIV} = 8$ $(pix/frame)$	0.6588	0.3946	0.6452	0.423
	$U_{PIV} = 16$ $(pix/frame)$	0.6588	0.3946	0.6452	0.423
e_{ω_z} (s^{-1})		1.9063	1.9063	1.9063	1.9063

within about 3% of one another, the average of the calibrations for each medium was applied to the field. In cases C % D, a separate camera was dedicated to each medium, and the calibration discrepancy was not an issue.

Once the velocity fields were calibrated, other physical quantities could be investigated. A major quantity of interest when studying most fluid flows is vorticity, which is the curl of velocity. Vorticity provides information about the rotational component of the flow, and is defined as

$$\vec{\omega} = \vec{\nabla} \times \vec{u} \tag{2.16}$$

where $\vec{\nabla}$ is the gradient operator and $\vec{u}$ is the three-dimensional velocity. In the case of two-dimensional flow, only the z-component of vorticity is present and is given by

$$\omega_z = \frac{\partial v}{\partial x} - \frac{\partial u}{\partial y} \tag{2.17}$$

Simply because the PIV measurement used herein is a two-dimensional measurement technique doesn't mean that the flow of interest is in fact two-dimensional. However, lab–generated spilling breakers are largely two-dimensional until the beginning of toe motion and lab–generated plungers are largely two-dimensional until jet impact, so the calculation of vorticity assuming two-dimensional flow is valid until these points and still insightful thereafter.

Since air and water was processed all at once for cases A & B, the vector field was a fully populated matrix. In the calculation of vorticity, no distinction was made between air and water either for these two cases. Vorticity was calculated using the MatLab curl function, which uses a finite difference method to approximate the spatial derivatives in Equation 2.17. It is recognized that calculating vorticity on the entire field likely yields larger levels at the free-surface than if the air and water were treated separately, but, again, the data from cases A & B was not intended to focus on near-surface results, rather to provide an overall picture of the physics.

For cases C & D, the goal was to treat the water and air flow fields separately, and thus vorticity was calculated separately for each medium. Calculation of vorticity

using the velocity matrix output from DaVis would yield spurious results near the surface because vectors in the masked region of the images were zeroed. Therefore, vorticity was calculated using a method presented in Dabiri & Gharib [8], whereby the last valid vector in each column is used to replace all remaining vectors in that column, and vorticity is calculated on the resulting field. Valid vectors are defined as those generated from an interrogation window which has center coordinates that lie in one medium (air or water) and not in the masked portion of either image of an image pair. Vorticity values were actually calculated using a method presented in Raffel et al. [34] whereby the local circulation is calculated around a small square path (defined by nearest 8 neighboring PIV points) and divided by the area enclosed by the path. For this method of vorticity calculation, Raffel et al. estimate the uncertainty in vorticity as

$$e_{\omega_z} = 0.61 \frac{e_{U_{PIV}}}{\Delta x_{PIV}} \tag{2.18}$$

where $e_{U_{PIV}}$ is the uncertainty in raw PIV velocity vectors and Δx_{PIV} is the PIV grid spacing (same for x and y directions). The uncertainty in vorticity for the present study was 1.91 s^{-1}.

Chapter 3

Results and Discussion

The purpose of the results from these experiments are two–fold: 1.) Results from cases A & B were used to provide feedback for the development of the measurement technique, and 2.) All cases were used to elucidate the physics of the air and water flow associated with wave breaking in the absence of wind. Description of the results are provided in that context. For cases A & B, observations about the physical phenomena as well as reasoning for why and how to improve the experimental method are presented. For cases C & D, attention turns to physical insight gained from the data, particularly to new information revealed by improved methodology.

3.1 Presentation of the Data

Results from several timesteps for experimental cases A–D are presented. Focus is primarily given to the evolution of the velocity and vorticity fields. For each case, sequences of the vorticity and velocity fields from pre-breaking to post-breaking are shown to illustrate the development of the water and air flow fields. Particular timesteps of interest warrant further examination, and are expounded upon. Some comparisons are made to published work, but that is presented in Section 4. First, results for the spilling and plunging breakers of cases A & B are presented since these studies provided proof-of-concept for the air flow seeding technique and guided the direction of ensuing studies.

Rather than arbitrarily assigning a zero time, timesteps are referenced to the time of a physically meaningful event. For the spilling breaking waves, the time corresponding to the beginning of toe motion is considered to be time $t = 0$ s. For the plunging breaker, $t = 0$ s corresponds to the time at which the jet impacts the surface. The times of particular frames are referenced to time zero in terms of the period of the waves, as measured by the upstream gauges. For example, for a wave with a period $T = 500$ ms and a timestep 100 ms prior to $t = 0$, the time is -0.2T. All experimental cases studied had a wave period of $T = 500$ ms.

Several figures are used to show the evolution of each breaking wave. For each particular experimental case, the same vorticity contour levels and color schemes are applied to the air and water, and are the same for each timestep. Therefore, the vorticity colorbar is displayed only with the first figure in a sequence, but applies to the rest of the figures corresponding to the same wave. Also, for ease of viewing, the axes are only applied to a pair of images on the first sequence, but axes are constant for all plots corresponding to a given wave.

3.2 Results for Spilling Breaking Wave in Case A

This section focuses on the spilling breaker from experimental case A. The sequences discussed in this section were chosen because they correspond to points of interest in the breaking process. The perceived orientations of the free-surface for time steps corresponding to pre-breaking and breaking are shown in Figure 3-1. At time t = -0.348 T, the crest is still symmetric. As the wave progresses along the shoal, the front face of the crest becomes steeper than the back. By time t = -0.048 T the surface displays a prominent feature of spilling breakers, with a pronounced bulge-toe structure on the front face. The capillary waves seen leading the toe in the spillers in Duncan et al. [11] are not evident here, likely due to the masking by the meniscus for this particular case. The toe is moving down the front face at time $t = 0.012$ T, and at time $t = 0.132$ T ripples are evident on the front face between the toe and crest, similar to what was seen in Duncan et al. [11].

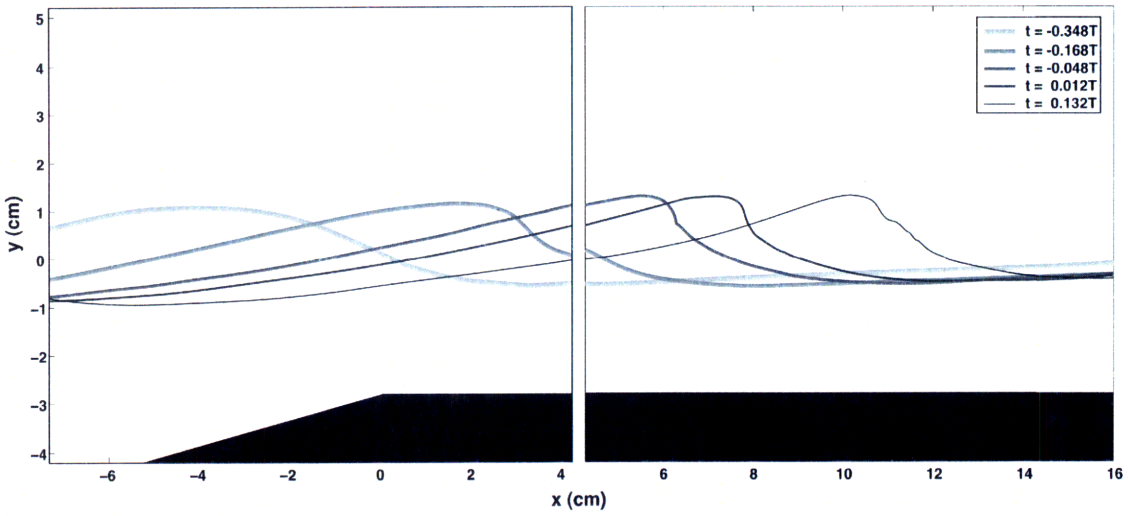

Figure 3-1: Free surface evolution for the spilling breaking wave in Case A. Timesteps were selected to show the wave at significant points during breaking.

Figure 3-2 shows the time evolution of velocity and vorticity for the spilling wave at times t = -0.348 T, t = -0.228 T and t = -0.108 T. The x-axis origin corresponds to the corner of the shoal, and the y-axis origin is the resting mean water level (MWL). At time t = -0.348 T, the velocity vectors are reminiscent of those one would find in a linear non-breaking wave. Almost no vorticity exists in the water, except near the top of the crest, which is due to the apparent shear layer induced by the water and air velocity vectors which are in the opposite direction. The water side of the flow at this time seems to be consistent with the fact that linear waves are irrotational. In the air flow above the crest, there is a region of moderate positive (clockwise) vorticity. On the forward face of the crest, there is a region of moderate negative (counterclockwise) vorticity, as the advancing wave crest forces the air flow up and to the right. As the crest moves to the plateau of the shoal (t = -0.228 T), the wave becomes asymmetric with the front face of the crest steeper than the back face. The velocity in the water and air begins to increase in the vicinity of the front face. Still essentially no vorticity exists in the water side of the flow, but the vortical regions on the air side have intensified somewhat and gathered toward each other the front face. Time t = -0.108 T presents much the same phenomena, except for a steeper front face and more intense air vorticity.

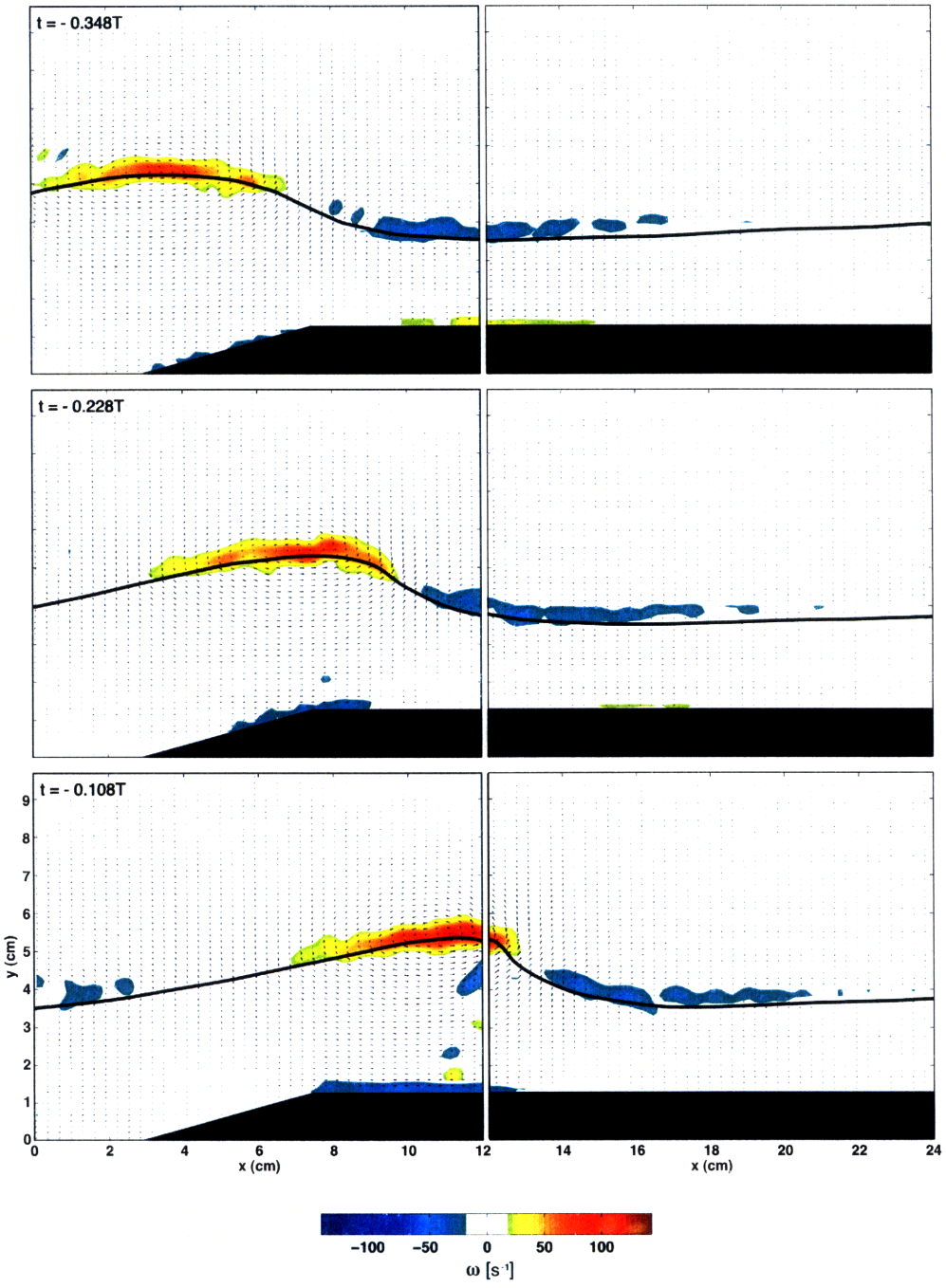

Figure 3-2: Velocity and vorticity for t = -0.348 T, t = -0.228 T and t = -0.108 T for the spilling breaking wave in Case A.

Figure 3-3 shows the time evolution of velocity and vorticity for the spilling wave at times $t = 0.012\ T$, $t = 0.132\ T$ and $t = 0.252\ T$. The axes and vorticity contours for these plots are the same as for Figure 3-2, but are not shown for clarity. Time $t = 0.012\ T$ corresponds to a time shortly after the onset of toe motion. The water velocity beneath has accelerated and a region of negative vorticity appears just to the left of the toe, although this observation requires more data to confirm due to the streaking. Later results for cases C & D will confirm this behavior. The region of positive vorticity in the air above the crest is very intense now as the progressing steep front face forces the air directly in front of it to move to the right and the air just above the crest moves to the left. The negative patch of vorticity in the air ahead of the crest has also intensified. The ripples on the face between the toe and the top of the crest at time $t = 0.132\ T$ are evidence of a shear layer that exists in the water side of the flow that was observed in Duncan et al. [11]. However, the vorticity in the water does not reflect the strong shear layer, and this is due to the masking by the meniscus. Fortunately, much of the air flow in the crest region can still be resolved as the masking is not as bad on the air side. The region of positive vorticity above the crest now stretches down toward the toe and the negative vorticity is still evident above and to the right of the toe. Thus far, the vorticity in the air flow has remained fairly close to the surface. However, at time $t = 0.252\ T$, a patch of positive vorticity extends in the air flow off the backside of the crest. The water side of the flow has become turbulent in the crest at this point, further exacerbating the meniscus masking problem. It is difficult to say anything conclusive regarding the water flow from this point forward.

Vorticty post-breaking is shown in the sequence of Figure 3-4. At $t = 0.372\ T$, there is still evidence of strong counter clockwise vorticity attached to the top of the crest. Also, some counter clockwise vorticity is shedding off the crest into the air flow. Finally , at $t = 0.492\ T$ and $t = 0.612\ T$, the region of positive vorticity has rolled up into a coherent vortex and shed completely from the back of the crest. This coherent structure was observed to repeatably form for all other spilling breakers cases studied, and is considered a mechanism for energy and momentum transport.

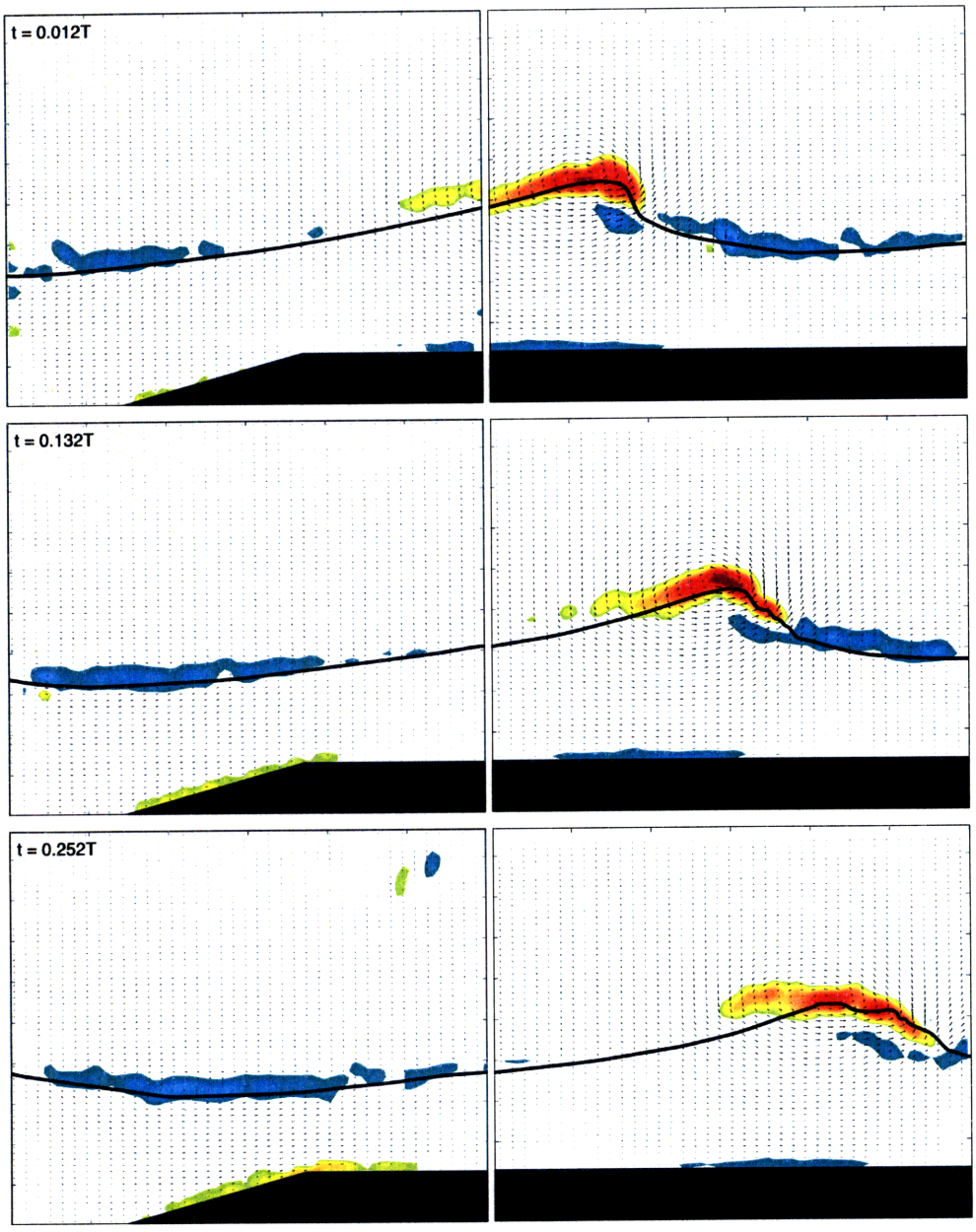

Figure 3-3: Velocity and vorticity for times $t = 0.012\ T$, $t = 0.132\ T$ and $t = 0.252\ T$ for the spilling breaking wave in Case A. Axes and vorticity contours are the same as figure 3-2.

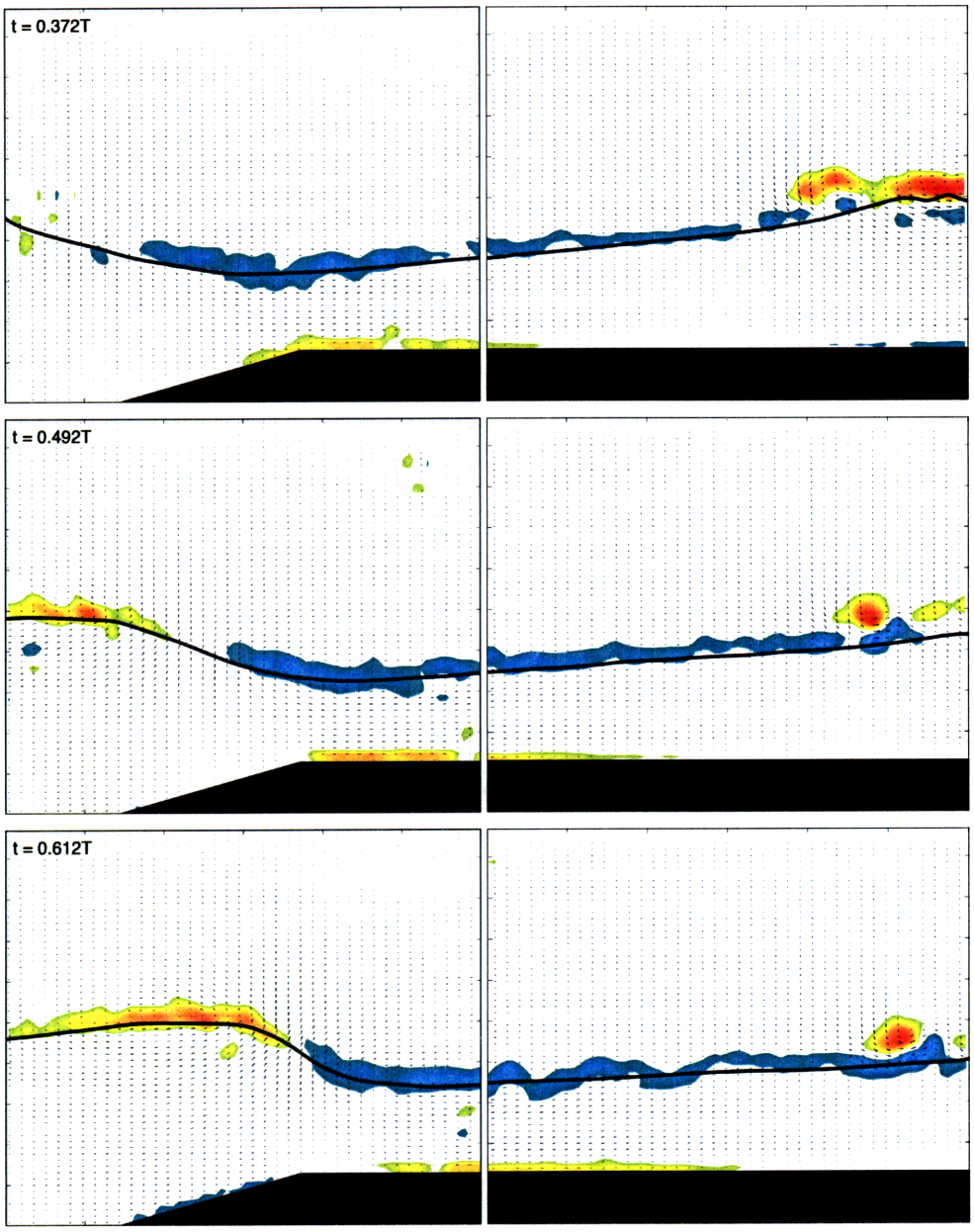

Figure 3-4: Velocity and vorticity for times $t = 0.372\ T$, $t = 0.492\ T$ and $t = 0.612\ T$ for the spilling breaking wave in Case A. Axes and vorticity contours are the same as figure 3-2.

This experiment elucidated some phenomena of interest and defined the regions of the flow that require detailed attention in the ensuing studies. The air-side vorticity intensifies steadily throughout the breaking process until finally vorticity sheds into the air. Capture of the air flow separate from the water flow will enable better investigation of near-surface vorticity in the air, without influence of the water veolcity in the vorticity calculations. Also, it is clear that the most interesting part of the water flow throughout the breaking process is at the front face of the crest between the toe and the top of the crest. Much of the detail was lost due to the masking by the meniscus, but these details become more clear in the results for cases C & D.

3.3 Results for Plunginig Breaker in Case B

This section focuses on the plunging breaker from experimental case B. Figure 3-5 shows the time evolution of velocity and vorticity for the plunging wave at times t = -0.328 T, t = -0.208 T, t = -0.088 T and t = 0.032 T. As the wave approaches the plateau of the shoal, the front face of the crest is clearly much steeper than the spilling wave in case A. A region of strong counter clockwise vorticity is attached to the top of the crest in the air side at t = -0.328 T and t = -0.208 T. On the lower portion of the front face resides strong negative vorticity that extends several centimeters to the right of the crest. Very little vorticity exists in the water at these timesteps. The free-surface has overturned by t = -0.088 T, and a large jet emanates from the top of the crest, clearly defining the wave as a plunging breaker. The velocity magnitudes in the water side are largest in the jet, and the positive vorticity is due to the apparent shear layer between the right-moving water and left-moving air above. The velocity in the air to the right of the jet is very large and the region of negative vorticity on the front face is stronger as the air flow gets rolled up beneath the jet. Finally, at t = 0.032 T, the jet has impacted the surface and a region of negative vorticity appears beneath the impact point. Above the crest, positive vorticity begins to shed into the air flow.

Figure 3-6 shows the plunging wave at times t = 0.152 T, t = 0.272 T, t = 0.392

T and $t = 0.512\ T$. The negative vortical region observed at $t = 0.032\ T$ penetrates deeper into the water, mixing the flow. A large coherent region of positive vorticity appears on the back of the crest at $t = 0.152\ T$ and $t = 0.272\ T$. The air and water flow induced by the plunging breaker is far more chaotic than the spiller, as the plunger induces more turbulence and dissipates more energy. Several other counter–clockwise vortices appear in the air flow at times $t = 0.272\ T$, $t = 0.392\ T$ and $t = 0.512\ T$, as opposed to the single coherent vortex observed for the spilling breaker in case A. At $t = 0.272\ T$, the turbulence has propagated in the water all the way down to the shoal, and in ensuing time the vorticity diffuses as energy dissipates.

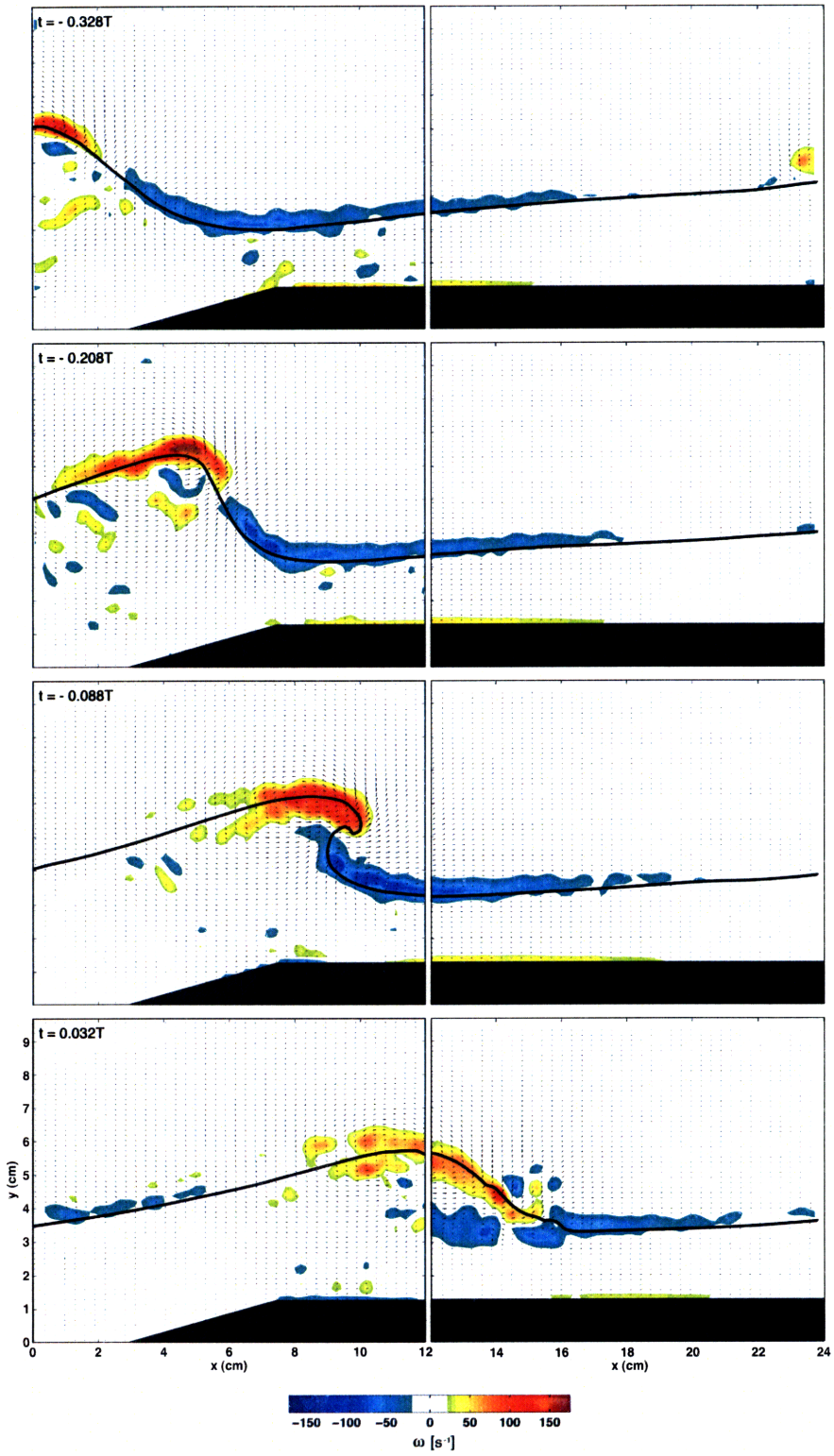

Figure 3-5: Velocity and vorticity for times t = -0.328 T, t = -0.208 T, t = -0.088 T and t = 0.032 T for the plunging breaker in case B.

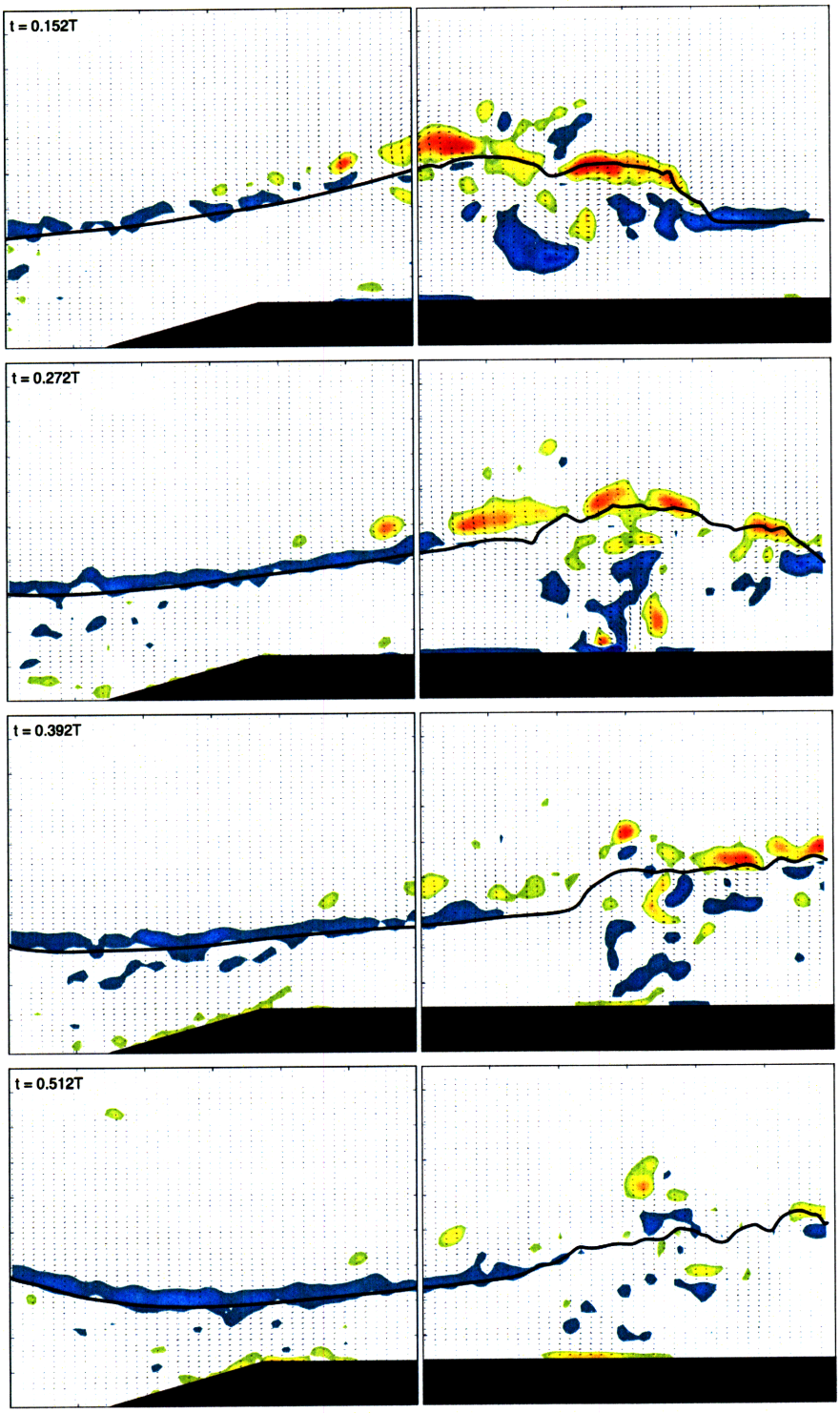

Figure 3-6: Velocity and vorticity for times $t = 0.152\ T$, $t = 0.272\ T$, $t = 0.392\ T$ and $t = 0.512\ T$ for the plunging breaker in case B. Axes and vorticity contours are the same as figure 3-5.

3.4 Results for Spilling Breaking Wave in Case C

Experimental case C constitutes the first results from the angled camera setup used to reveal near-surface data by avoiding masking from the wall meniscus. The vorticity and velocity fields for the air and water are shown in Figures 3-7 – 3-9, with water plots shown in the left column and air plots at the same timestep shown in the right column. Although the timesteps of air and water plots are identical, the FOV for each camera was different, and is reflected in the vorticity and velocity plots. The corner of the shoal corresponds to x = 0, and the y-axis origin is the resting mean water level (MWL). Also, the free-surfaces for each timestep were defined separately for the air and the water, and variation in the details of the surface geometry was unavoidable. However, the surfaces are used to compare the flow fields with the stage of breaking, thus the variations are unimportant. In the discussion of the ensuing figures, attention is paid to flow features unveiled through use of the angled camera setup, rather than reiterating similar flow features observed for the spilling breaker in case A.

Figure 3-7 shows the evolution of the spilling breaker before toe motion. At t = -0.168 T and t = -0.120 T, the only appreciable vorticty in the water resides on the shoal. On the air side, very low levels of positive vorticty exist on the top of the crest, and low levels of negative vorticity appear near the toe and in the trough. The water vorticity and velocity at time t = -0.072 T reveals some new information. Just left of where the toe has formed, a distinct isolated region of negative vorticity appears. The velocity vectors indicate an increase in velocity magnitude and change in direction near the toe, generating this vorticity. At t = -0.024 T, toe motion is imminent, and the curvature near the toe is much shaper now. The region of negative vorticity shows increased magnitude and stretches from beneath the toe to high on the front face of the crest. At this time, the positive vorticity in the air on the top and backside of the crest is more evident as the air flow is forced up and over the crest and then reverses direction about 3 cm down the backside of the crest from the top. The negative vorticity at the toe in the air also shows larger magnitude as the

crest steepens and the toe sharpens. It is worth noting that capillary waves are not evident in the prior timesteps discussed, and this is likely because the capillaries are too small to be resolved given that this is a very gentle spiller.

The evolution of the velocity and vorticity of the spiller post-toe motion is shown Figure 3-8. The prominent feature in the water flow at time $t = 0.024\ T$ is still the region of strong negative vorticity stretching from the toe to the top of the front face of the crest. The air flow looks essentially the same as for time t = -0.024 T. At t = 0.072 T the ripples that appear on the crest after toe motion as noticed in Duncan et al. [11] are evident. The negative vorticity in the water flow is still intense, but does not penetrate very deep into the flow. In the air flow, the only change to speak of is the diminishing value of the negative vorticity on the front face from time $t = 0.072$ T until the toe leaves the field of view. The water flow becomes more turbulent at times $t = 0.120\ T$ and $t = 0.168\ T$ in the crest region. Still, the region of negative vorticity is confined to within about 1 cm of the surface. Positive vorticity stretching from the top of the crest well down the backside is still the prominent feature in the air flow.

The air flow really becomes interesting at times after the crest becomes turbulent. Figure 3-9 shows the evolution of the spiller after turbulence consumes the top of the crest. The interesting features of the water flow are largely outside the field of view at this time. At $t = 0.216\ T$ significant positive vorticity exists just behind the top of the crest as the point of air flow reversal now is only about 1.5 cm down the backside of the crest with respect to the top. The positive vorticity persists at time $t = 0.264$ T, and stretches over a larger portion of the backside.

Figure 3-10 further highlights the evolution of the air flow. At $t = 0.288\ T$, the region of positive vorticity is beginning to roll up into a coherent vortex. The vortex roll up continues through the remaining timesteps. Although the wave exits the field of view, it is likely that this coherent structure fully separates from the backside of the crest and lingers in the air flow, based on the observations for the spiller in case A.

Using a method presented in Qiao & Duncan [11] whereby the velocity vectors

are plotted in a crest–relative reference frame can provide further insight into the flow physics. In order to do this, Qiao & Duncan subtract the local crest speed from the u–component of velocity. First, the local crest speed must be established. In the present study, this was accomplished by shifting the hand–selected surfaces until they visually aligned. Figure 3-11 shows a plot of the surfaces for the spiller at times t = -0.008 T, t = -0.004 T and t = 0 T. The bottom plot shows the surfaces shifted to align with one another. By shifting surfaces for several times corresponding to the lead–up to breaking to just after toe motion, the local crest velocity can be established. It was found that between times t = -0.208 T and t = 0.12 T the crest speed was fairly constant, with an average speed of $U_{crest} = 50.4\ cm/s$ and standard deviation of 1.96 cm/s.

Qiao & Duncan claim that the spilling breaking process coincides with a reversal of the water flow in a crest–relative reference frame. In other words, the velocity of the fluid exceeds the crest speed. For the spiller in case C, at only one time and location did the water flow actually reverse direction in a crest–relative frame. This vector is shown the left–hand plot of Figure 3-12, and the right–hand plot shows the velocity field in a crest–relative frame. In order to investigate whether the flow repeatably reverses upon breaking, repeated higher resolution experiments in the water side of the flow would be necessary.

Figure 3-13 shows the spilling breaker at t = -0.048 T and t = 0 T where $U = 0.5U_{crest}$ has been subtracted from the u–component of the velocity field. This method of plotting helps reveal the rotational component of the flow in the near crest region which was seen earlier in the vorticity fields.

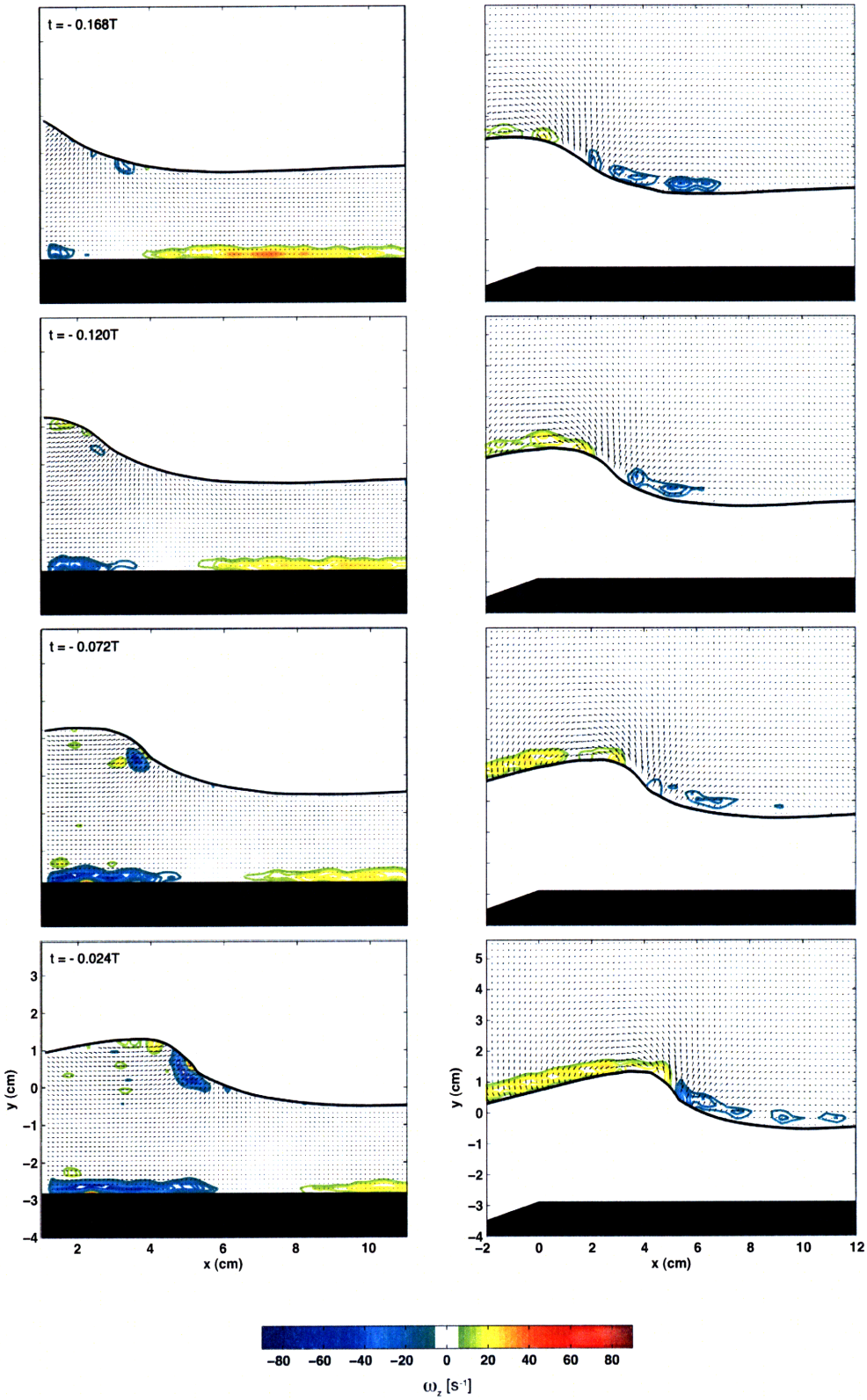

Figure 3-7: Velocity and vorticity for spilling breaker from case C at times t = -0.168 T, t = -0.120 T, t = -0.072 T and t = -0.024 T.

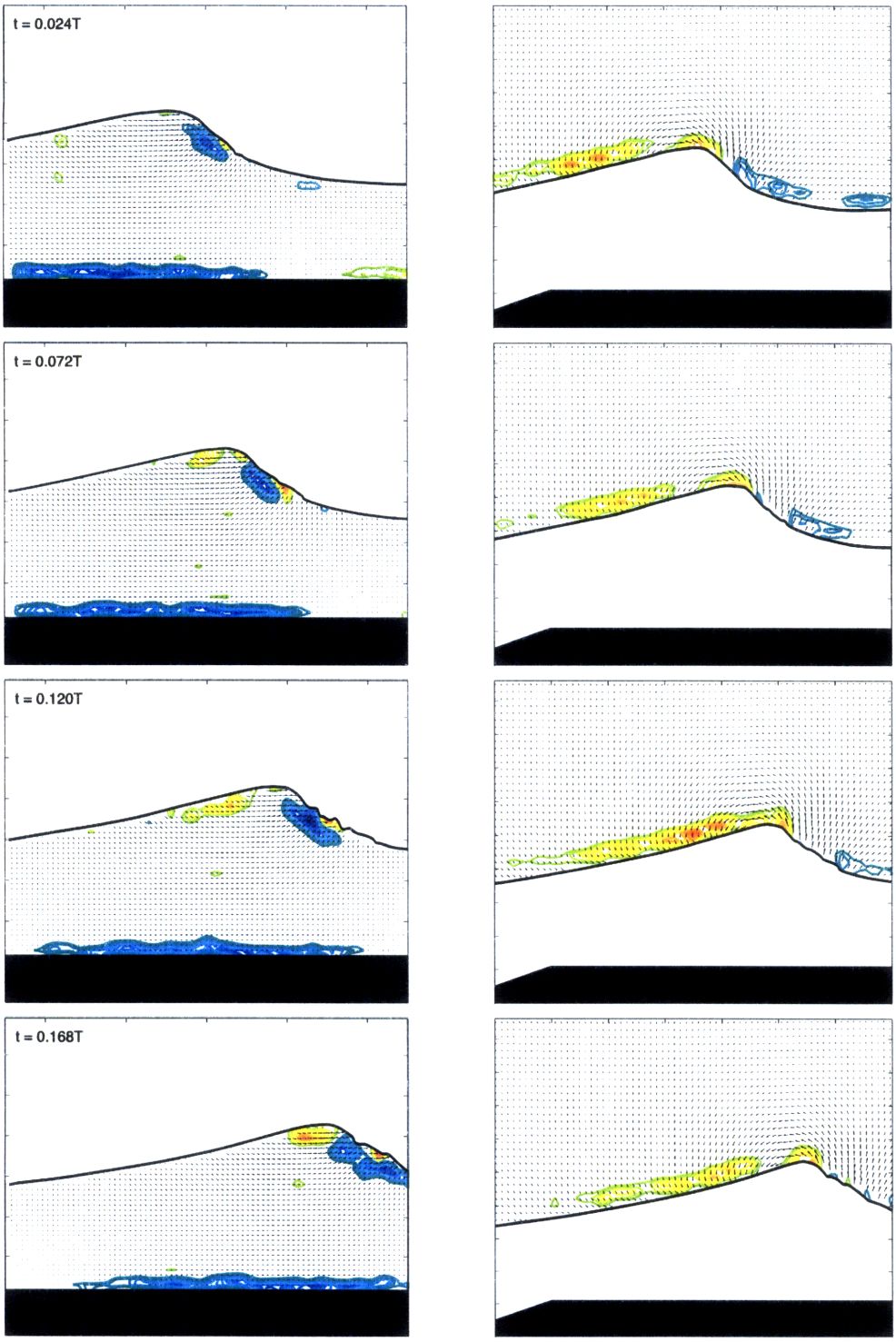

Figure 3-8: Velocity and vorticity for spilling breaker from case C at times $t = 0.024$ T, $t = 0.072$ T, $t = 0.120$ T and $t = 0.168$ T. Axes and vorticity contours are the same as figure 3-7.

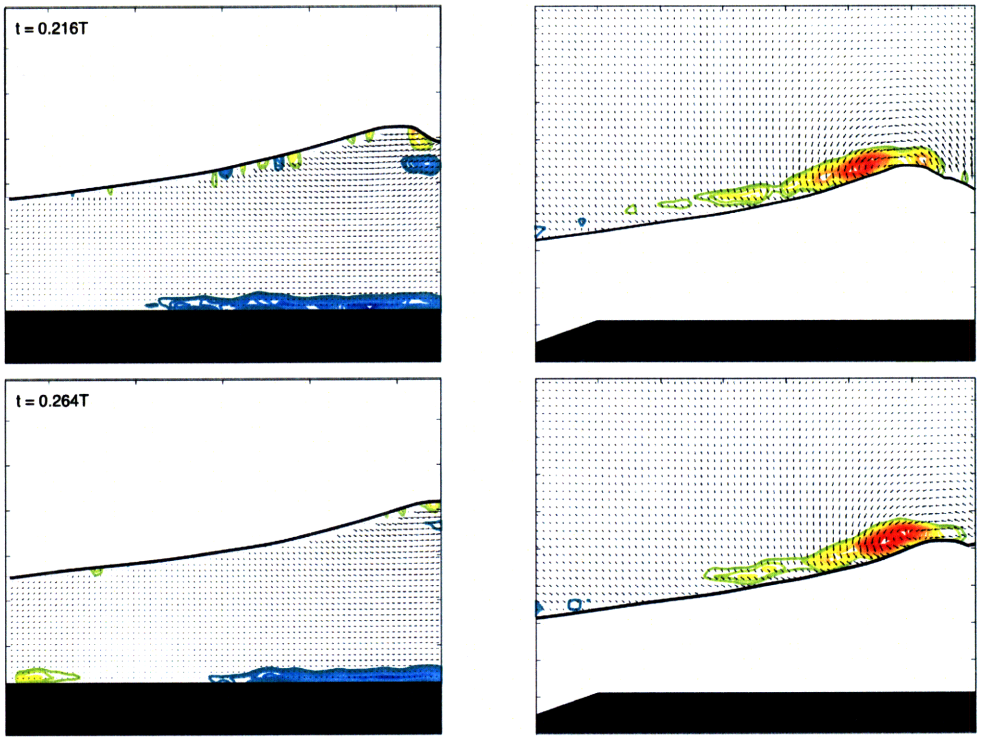

Figure 3-9: Velocity and vorticity for spilling breaker from case C at times $t = 0.216$ T and $t = 0.264$ T. Axes and vorticity contours are the same as figure 3-7,

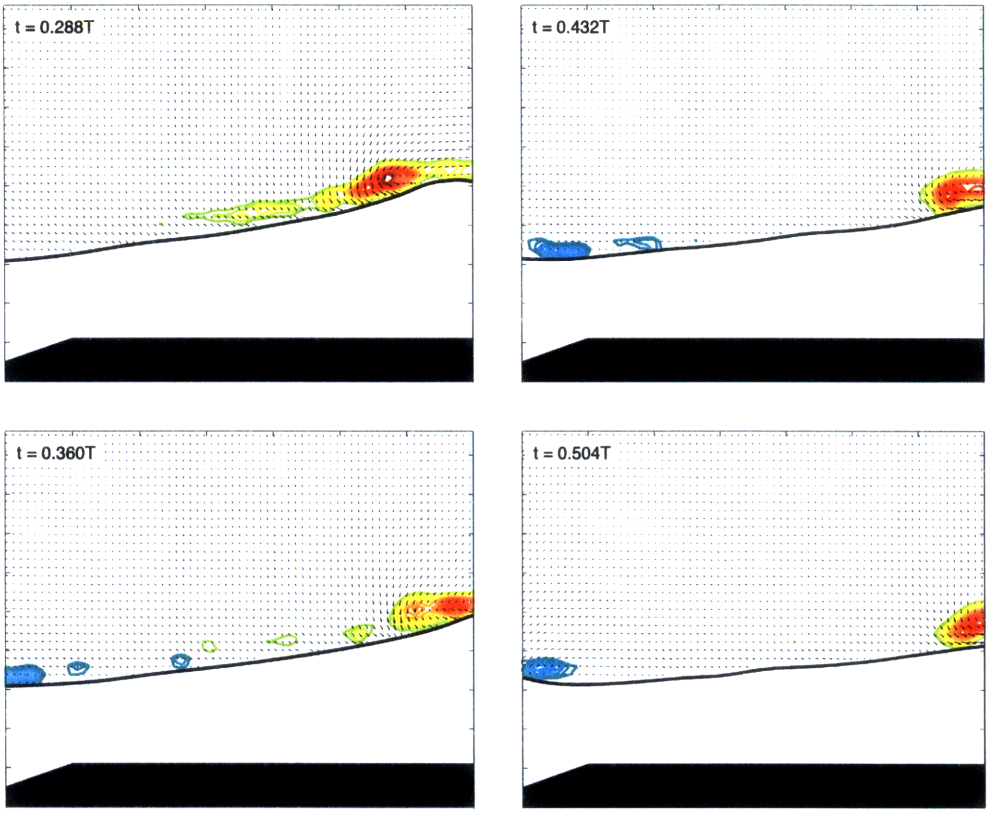

Figure 3-10: Velocity and vorticity for the air side of the spilling breaker from case C at times $t = 0.288\ T$, $t = 0.360\ T$, $t = 0.432\ T$ and $t = 0.504\ T$. Axes and vorticity contours are the same as figure 3-7.

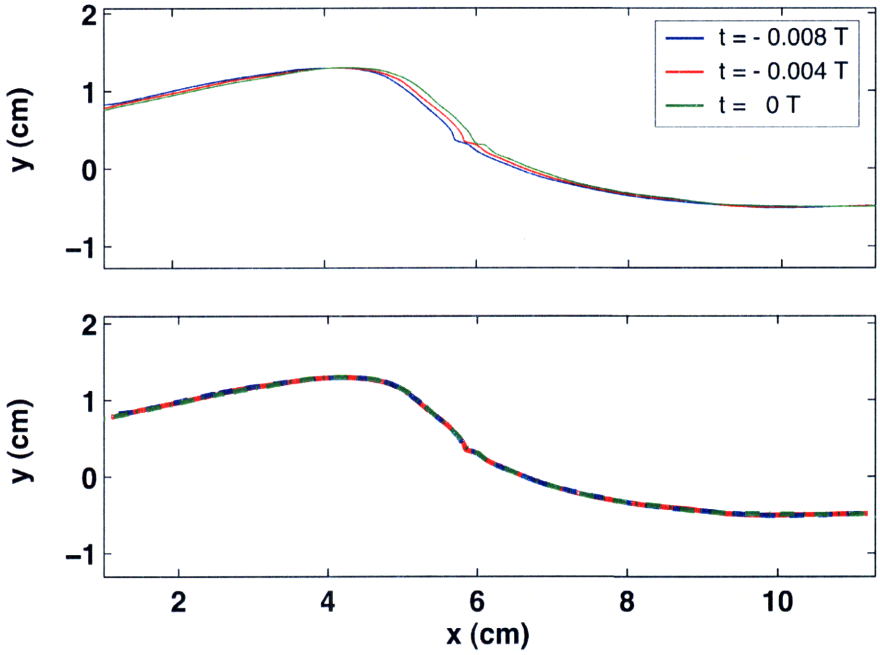

Figure 3-11: Top plot shows the orientation of the free–surface at times t = -0.008 T, t = -0.004 T and t = 0 T. Bottom plot shows the surfaces shifted to align with one another.

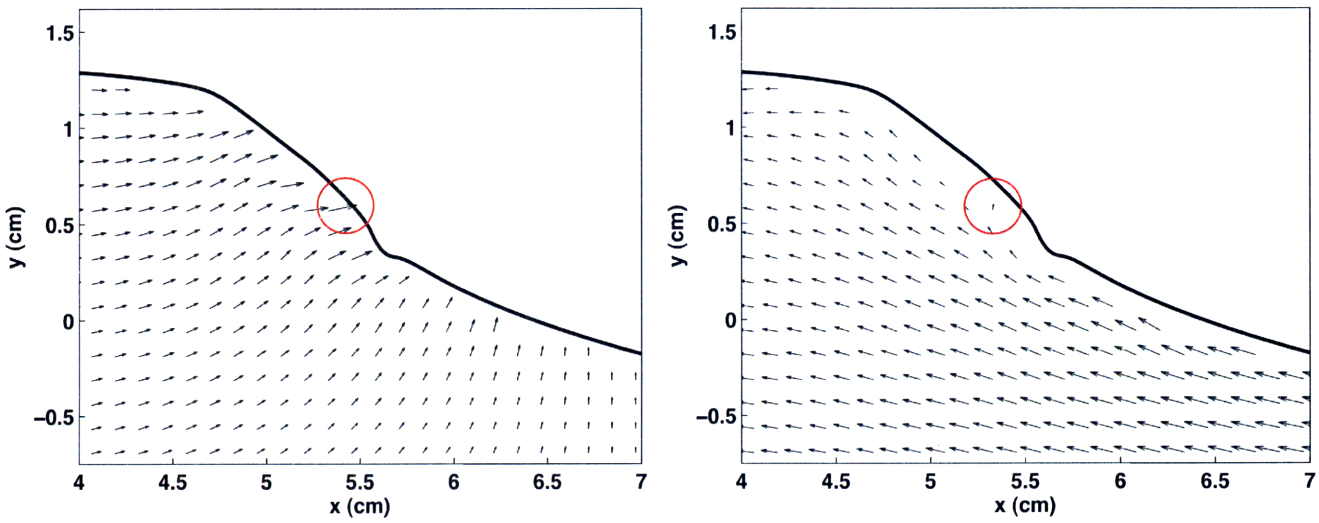

Figure 3-12: Spilling breaker in case C at time t = -0.012 T. Left image shows the location of maximum velocity in the crest. Right image shows velocity in crest-fixed coordinates.

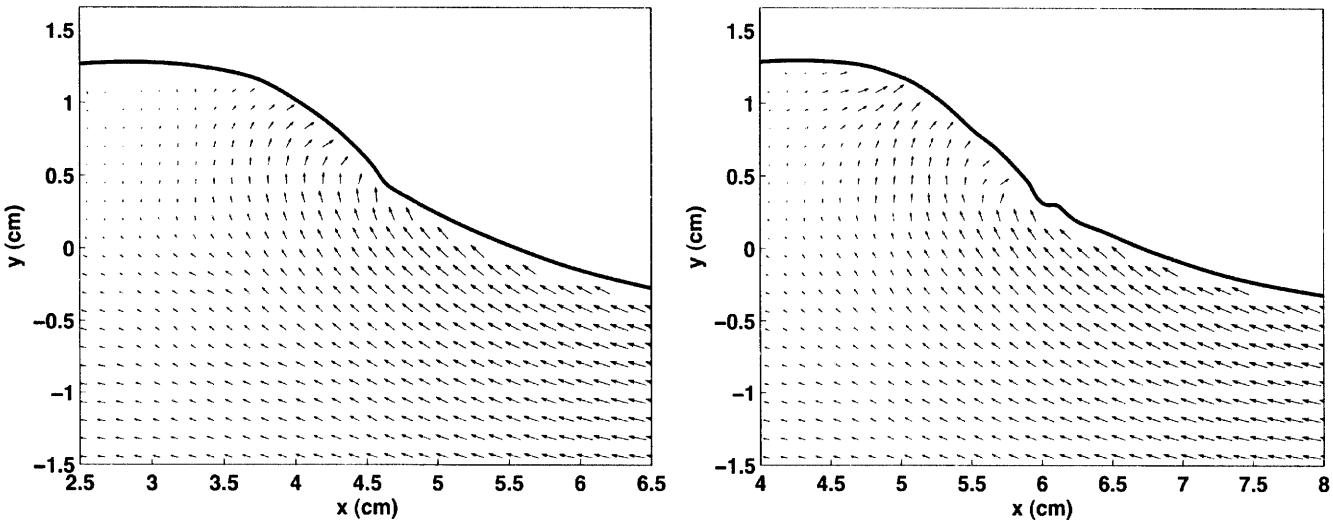

Figure 3-13: Spilling breaker in case C at times t = -0.048 T (left) and t = 0 T (right). One-half of the local crest velocity has been subtracted from the velocity fields to reveal the rotationality of the flow near the crest.

3.5 Results for Spilling Breaking Wave in Case D

Experimental case D applied the same angled camera technique used for case C to a spilling breaker with different surface tension. The different value of surface tension changed the breaking characteristics. Rather than repeating redundant characteristics from case C in the following description, differences and unique features of the flow fields associated with the spiller in case D will be highlighted.

Figure 3-14 shows the evolution of the spiller pre–toe motion. The crest becomes much steeper prior to breaking than the spiller observed in case C. Also, the capillary waves are much more pronounced in the present breaker, particularly at t = -0.040 T. At this time, the classic bulge-toe system is very evident. Interestingly, no negative vorticity appears in the water side of the wave prior to toe motion. In case C, significant negative vorticity appeared in the water near the toe as early as t = -0.072 T. Qiao & Duncan [11] observed no significant vorticity in the water prior to toe motion for the spilling breakers they investigated. In order to further investigate this issue, higher resolution of the water flow fields would likely be required, because the patches of vorticity that appear in the water extend over regions of tenths of centimeters where only a few velocity vectors are available. The overall characteristics of the flow appear to be captured with the present experiments, but the details of the origin of vorticity, in both space and time, appear to require closer investigation.

Figure 3-15 shows the evolution of the spiller post–toe motion. The negative vorticity region emanates from the toe at the time just after toe motion begins, and spreads as the toe moves down the front face. The air flow structure is qualitatively similar to that for case C. All vorticity levels, both in the air and water, are larger than for case C, which is consistent with the steeper face and more pronounced bulge-toe structure in the lead–up to breaking. Figure 3-16 shows the wave leaving the FOV in the water; the crest is likely turbulent at this time. In the air, the flow reverses and strong positive vorticity resides on the backside of the crest.

Figure 3-17 shows the evolution of air flow for several more timesteps. These snapshots show the separation of the coherent vortex from the backside of the crest,

and the roll–up of this structure. The vortex lingers in the air flow, and induces a region of negative vorticity just to the right of the coherent structure. These vorticity fields show that this coherent structure stimulates mixing of the air flow in the wake of a spilling breaker.

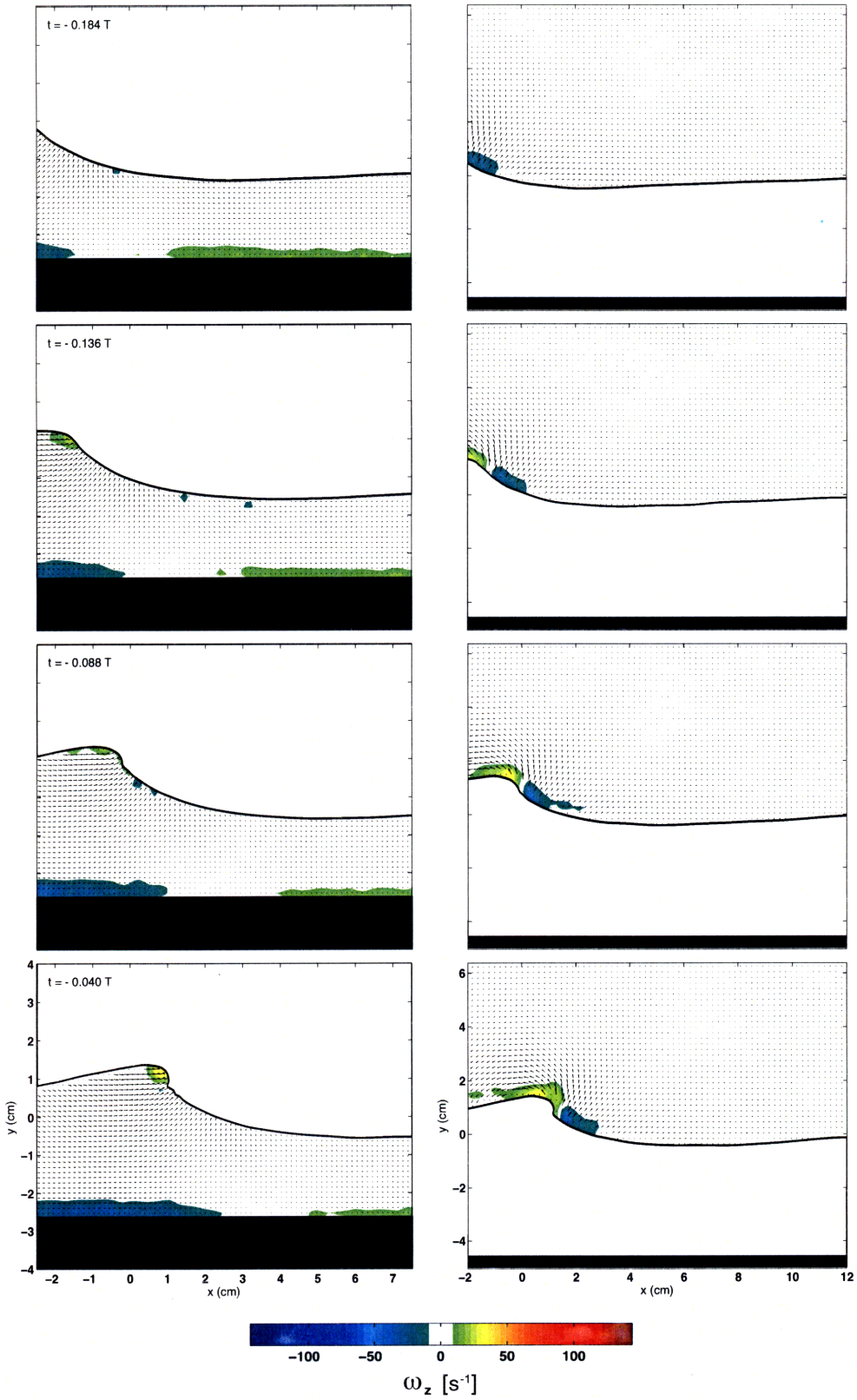

Figure 3-14: Velocity and vorticity for the spilling breaker from case D at times t = -0.184 T, t = -0.136 T, t = -0.088 T and t = -0.040 T.

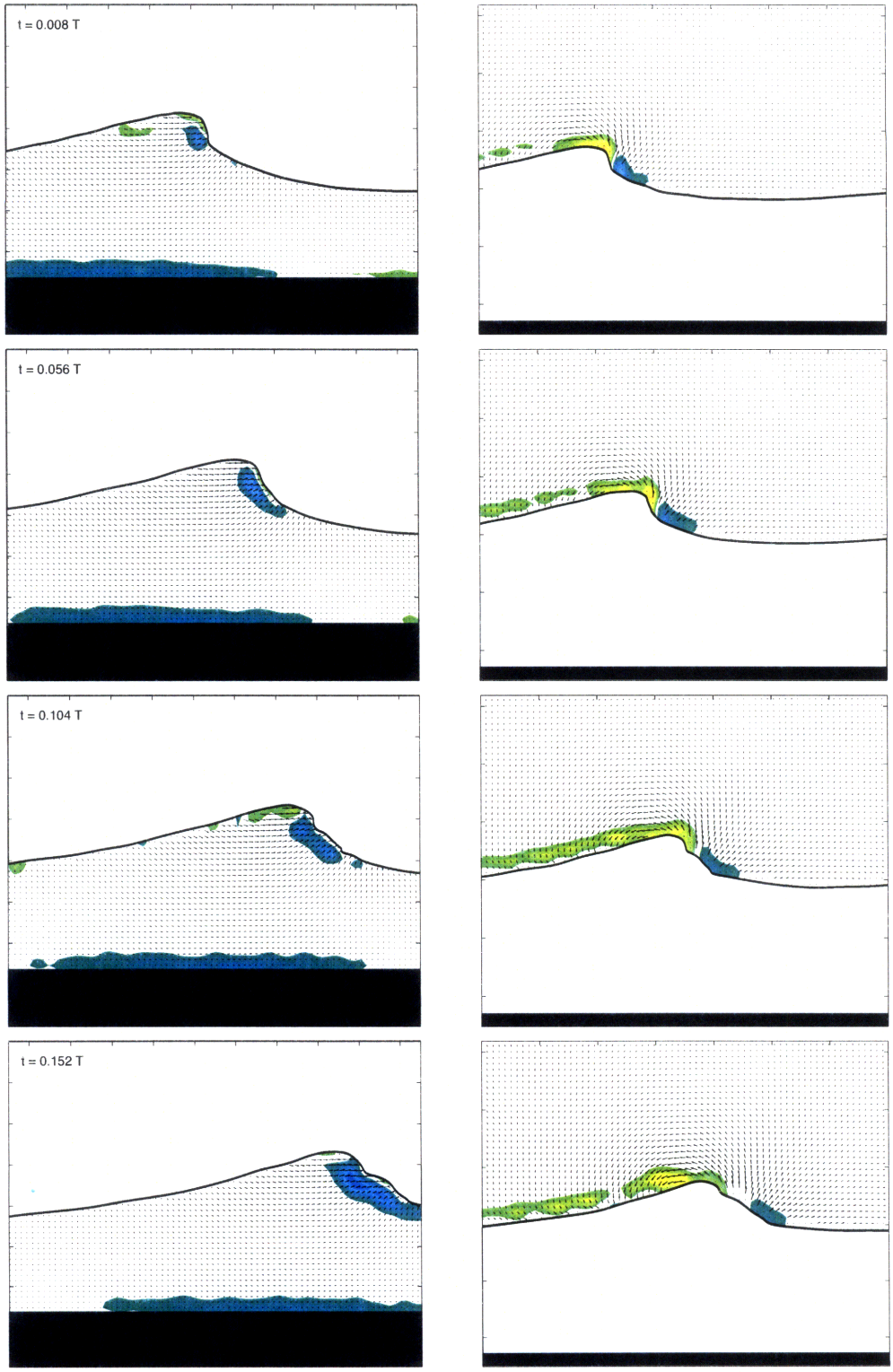

Figure 3-15: Velocity and vorticity for the spilling breaker from case D at times $t = 0.008\ T$, $t = 0.056\ T$, $t = 0.104\ T$ and $t = 0.152\ T$. Axes and vorticity contours are the same as figure 3-14.

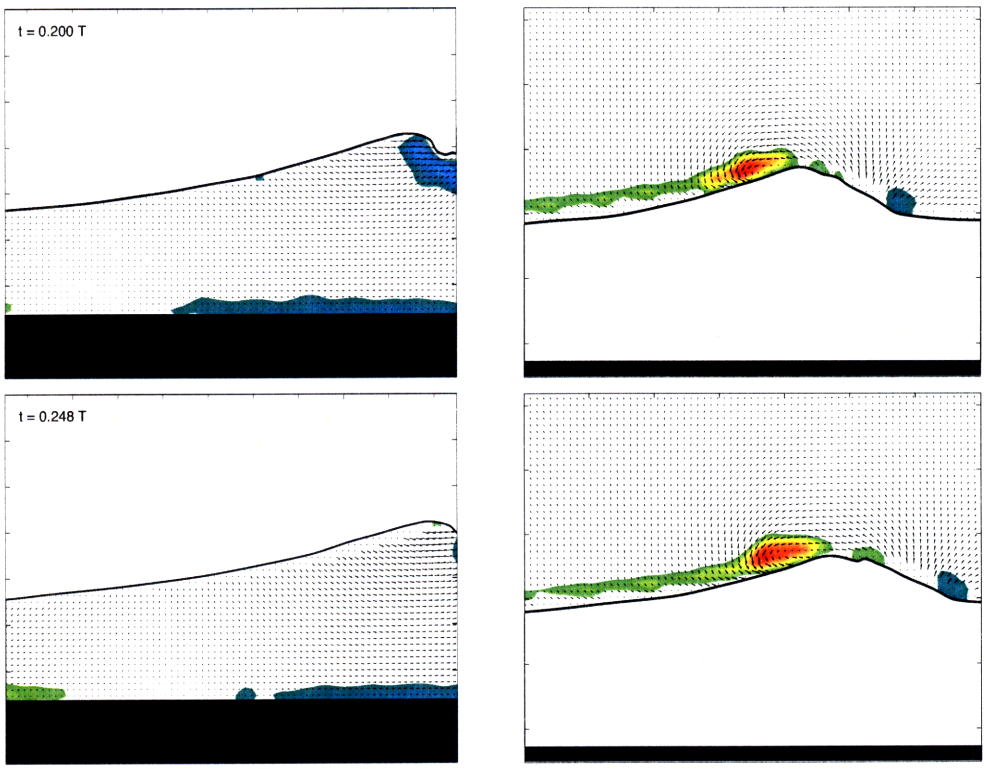

Figure 3-16: Velocity and vorticity for the spilling breaker from case D at times $t = 0.200\ T$ and $t = 0.248\ T$. Axes and vorticity contours are the same as figure 3-14.

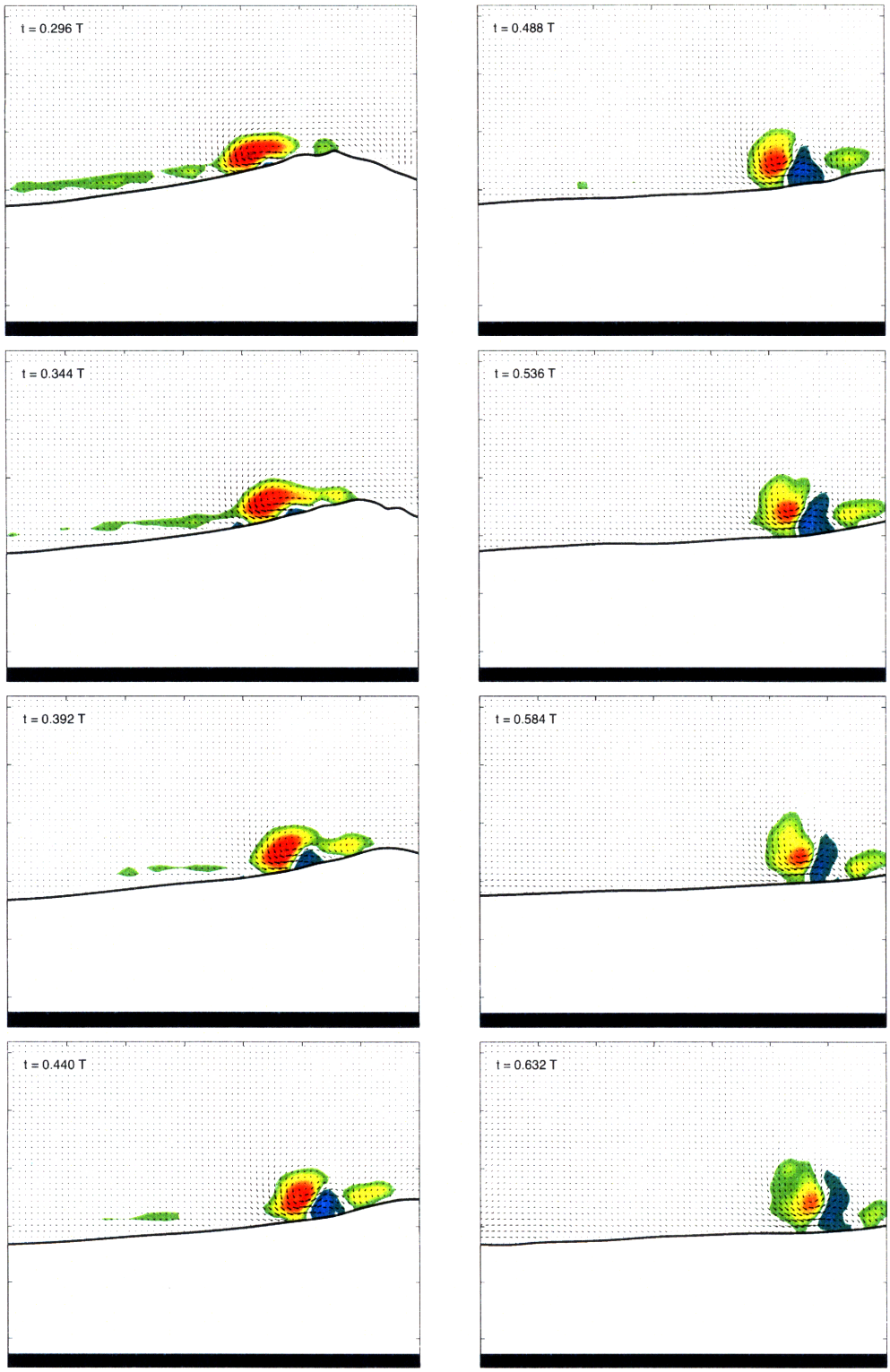

Figure 3-17: Velocity and vorticity for the air side of the spilling breaker from case D at times $t = 0.296\ T$ through $t = 0.632\ T$ with a spacing between frames of $t = 0.048\ T$. Axes and vorticity contours are the same as figure 3-14.

Chapter 4

Conclusions

A method for simultaneously capturing the air and water flow fields induced by wave breaking has been developed and presented. The method makes use of novel air flow seeding to enable PIV measurements in quiescent air. High–speed quantitative PIV imaging allows for fully time resolved capture and quantification of the velocity fields associated with plunging and spilling breakers. Extensive experimentation with camera placement revealed that simultaneous capture of air and water data on one CCD camera is possible with the limitation of masked near–surface data due to the meniscus formed on the near tank wall. Angling the cameras allows for capture of one medium of the flow field without masking, thus enabling near–surface measurements. The method has been used to study the air and water flow fields associated with spilling and plunging breakers. The breaking process indeed has a profound impact on the air flow structure, inducing significant vorticity in the air above.

In order to place this work in a greater context, qualitative comparison is drawn with the experimental work of Qiao & Duncan [11]. Qiao & Duncan used PIV to investigate the water flow field induced by dispersively generated spilling breakers. Figure 4-1 shows several snapshots for the spiller in Qiao & Duncan, as well as snapshots of the spillers from cases C & D in the present work. Figure 4-1(a)–(c) are reprinted from Qiao & Duncan, who reference the breaking stages not by time, but by distance from wavemaker. Therefore, it is not possible to directly compare across timesteps, but it is still useful to draw qualitative comparisons. In Figure 4-1(a),

Qiao & Duncan show the vorticity field just after toe motion. Figure 4-1(d)&(g) show the spilling breakers in cases C & D at times shortly after toe motion. In Figure 4-1(a)&(g), similar low levels of vorticity appear near the toe, while in Figure 4-1(d) a larger and relatively more intense region of vorticity is observed. This may be due to the fact that the breaking is at a later stage, but vorticity was observed to form earlier near the toe in case C than in case D. In Figure 4-1(b), Qiao & Duncan notice the toe moving down the front face and ripples on the crest; the vorticity is more intense and widespread. This flow structure is quite similar to that shown in Figure 4-1(e)&(h) from the spillers in the present work. Finally, Figure 4-1(c) shows the vorticity has spread more throughout the near–crest region, and Qiao & Duncan notice three distinct eddies in the flow. There is evidence of distinct eddies in Figure 4-1(f)&(i), indicating that similar physics occurs for the spillers presented herein. This qualitative comparison shows similarity between water flow structure, despite different scales of breaking and breaking generation methods.

While interesting physics has been revealed through this work, further examination is warranted. In the future, higher resolution near the surface in both the air and water may reveal more detailed information regarding flow separation, near–surface shear and velocity and other interesting details of breaking. Additionally, the origins of vorticity during breaking is a desirable, yet elusive measure when it comes to breaking waves. Dabiri & Gharib [8] measure the vorticity flux to examine sources of vorticity in the water side a steady spilling breaker, but similar measurements for unsteady breakers seem to be lacking. Measurements of vorticity flux on the air and water side of an unsteady breaker would provide useful insight, and will be the goal of future work. The technique presented in this work should further our knowledge in the important and difficult field of wave breaking. Hopefully, this is a stepping stone to unveiling more physics of wave breaking and its role in air–sea interaction, which will aid the scientific and engineering communities.

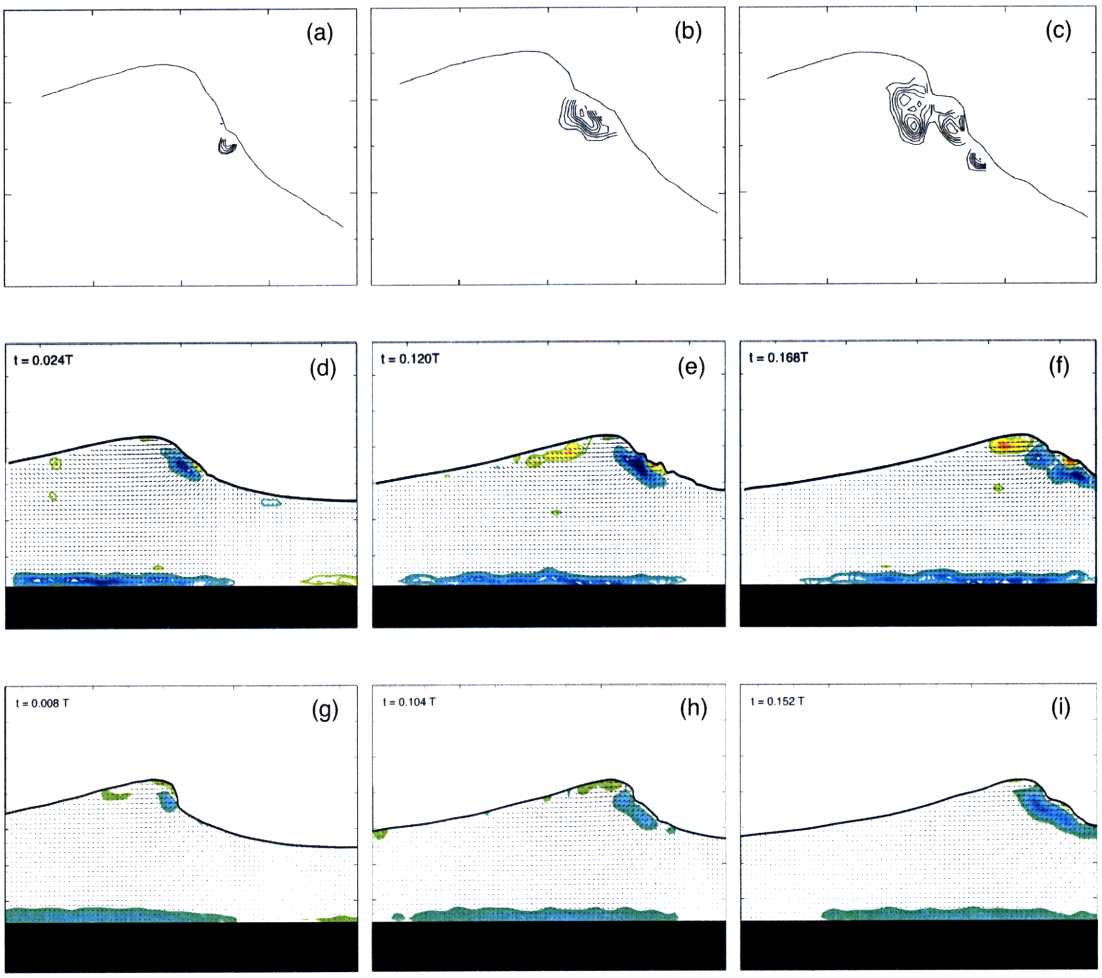

Figure 4-1: Plots (a)–(c) are reprinted from Qiao & Duncan [11], and show the vorticity contours for the spilling breaker they studied. Plots (d)–(f) are velocity and vorticity of the spilling breaker in case C at similar stages of breaking to those in plots (a)–(c). Plots (h)–(i) are velocity and vorticity of the spilling breaker in case D at similar stages of breaking to those in plots (a)–(c).

THIS PAGE INTENTIONALLY LEFT BLANK

Appendix A

PIV Error Analysis

Many factors contribute to error in PIV measurements. Raffel et al. [34] summarize thoroughly the sources of PIV error and evaluation thereof. In this section, the error due to PIV is evaluated and propagated to quantities of interest. The LaVision commercial software package DaVis 7.2 was used to perform the PIV velocity field measurements, and the error due to this algorithm has been investigated and summarized in Stanislas et al. [39]. For the present study, it is estimated that the error on the velocities due to the PIV algorithm for all cases is 0.1 pixels/frame, and this is likely a conservative estimate considering the results presented in Stanislas et al. [39]. In order to propagate the error from the raw data to the final velocity and vorticity fields, one must consider the error on the camera calibration as well as the PIV error. The camera spatial calibration, K_x, is defined by placing a calibration target in the camera FOV, and calculating the pixels spanned by a known distance on the target, and is calculated from

$$K_x = \frac{d}{\Delta pix} \tag{A.1}$$

where d is the known distance between two points on the calibration target and Δpix is the corresponding separation between the two points in image pixels. Two sources of error contribute to the camera calibration itself: the accuracy of the calibration target and the error in selection of pixels. The error on pixel selection is $\pm 1/2$

pixels, and the accuracy of the ruler used for the calibration target is estimated at ± 0.1 mm. The calibration actually requires two points to be selected, and thus the calibration error due to pixel selection is $e_{\Delta pix} = \pm 1$ pixels and the error due to the ruler is $e_d = \pm 0.1$ mm. The Kline–McKlintock method for error propagation, which is described in Figliola & Beasley [12], allows for propagation of error in measurements through to error on quantities calculated from these measurements. The general formula for the Kline–McKlintock method of error propagation to find the error on a calculated variable R is,

$$e_R = \pm \sqrt{\sum_{i=1}^{L} (\theta_i e_{x_i})^2} \tag{A.2}$$

where L is the number of variables, x_i is the ith input variable, and θ_i is given by

$$\theta_i = \left. \frac{\partial R}{\partial x_i} \right|_{x=\bar{x}} \tag{A.3}$$

where the derivative is evaluated at the mean value, $\bar{x}$, of the variable with which it was taken respect to. Applying Equations A.2 and A.3 to find the error on the camera calibration yields

$$e_{K_x} = \pm \sqrt{(\theta_d e_d)^2 + (\theta_{\Delta pix} e_{\Delta pix})^2} \tag{A.4}$$

Taking the appropriate partial derivatives, Equation A.4 becomes

$$e_{K_x} = \pm \sqrt{\left(\frac{1}{\Delta pix}\right)^2 + \left(\frac{-d}{\Delta pix^2} e_{\Delta pix}\right)^2} \tag{A.5}$$

In cases A & B, the camera calibrations used were the average of the calibration for air and water, and thus an additional term must be added to e_{K_x}. The error applied to these calibrations was

$$e_{K_{x\,AB}} = \pm \left(|K_x - K_{x ave}| + e_{K_x} \right) \tag{A.6}$$

where K_x is the actual camera calibration for the respective medium and K_{xave} is the average calibration that was applied.

Spatial coordinates were calibrated using

$$\Delta_x = \frac{\Delta_{xPIV}}{K_x} \tag{A.7}$$

where Δ_{xPIV} is the spacing of the PIV grid in pixels. This spacing is fixed and has no error associated with it. Using Equation A.2, the error on spatial distances is

$$e_{\Delta_x} = \pm \left(\frac{-\Delta_{xPIV}}{{K_x}^2} e_{K_x} \right) \tag{A.8}$$

Velocities output from the PIV algorithm have units of pixels/frame, and are converted to physical units using the formula

$$U = U_{PIV} \frac{K_t}{K_x} \tag{A.9}$$

where U_{PIV} is the velocity from the PIV algorithm and K_t is the conversion from frames to seconds and is equal to 500 frames/sec. Using Equation A.2, the error on velocity is

$$e_U = \pm \sqrt{\left(\frac{K_t}{K_x} e_{U_{PIV}} \right)^2 + \left(\frac{-U_{PIV} K_t}{{K_x}^2} e_{K_x} \right)^2} \tag{A.10}$$

The error on the velocity actually depends on the magnitude of the velocity from the PIV algorithm. Therefore, in the tables in Section 2.5, the velocity error corresponding to typical velocities of 4, 8 and 16 pix/frame are calculated.

As mentioned in Section 2.5, vorticity values are actually calculated using a method present in Raffel et al. [34] whereby the local circulation is calculated around a small square path (defined by nearest 8 neighboring PIV points) and divided by the area enclosed by the path. For this method of vorticity calculation, Raffel et al. estimate the uncertainty in vorticity as

$$e_{\omega_z} = \pm 0.61 \frac{e_{U_{PIV}}}{\Delta_{xPIV}} \tag{A.11}$$

Since the spatial coordinate drops out of the calculation of vorticity (units of vorticity are sec^{-1}), the error due to the camera calibration drops out. Thus, the error on vorticity is due only the error on velocity from the PIV algorithm.

Appendix B

Imaging Different Fluids With a Single Camera

In Section 2.4.3, the issue of change in effective FOV due to imaging air and water with a single camera was alluded to. This is due to a difference in the index of refraction between air and water. As shown schematically in Figure B-1, the light rays emanating from the object plane in the water bend away from the axis normal to the interface as they enter the air. At an interface between two different media, light rays refract according to Snell's Law, which is given by

$$n_1 sin\theta_1 = n_2 sin\theta_2 \tag{B.1}$$

where n is the index of refraction of the medium and θ is the angle between the light ray and the axis normal to the interface. For the object plane in air, the angle of light rays emanating from the object plane equals the angle of rays entering the camera, because the camera is in air. The camera's aperture is fixed, and for the sake of this discussion the largest angle of acceptance is α. Applying Snell's Law to a ray that emanates from the object plane in the water and enters the camera at an angle α yields

$$n_{water} sin\beta = n_{air} sin\alpha \tag{B.2}$$

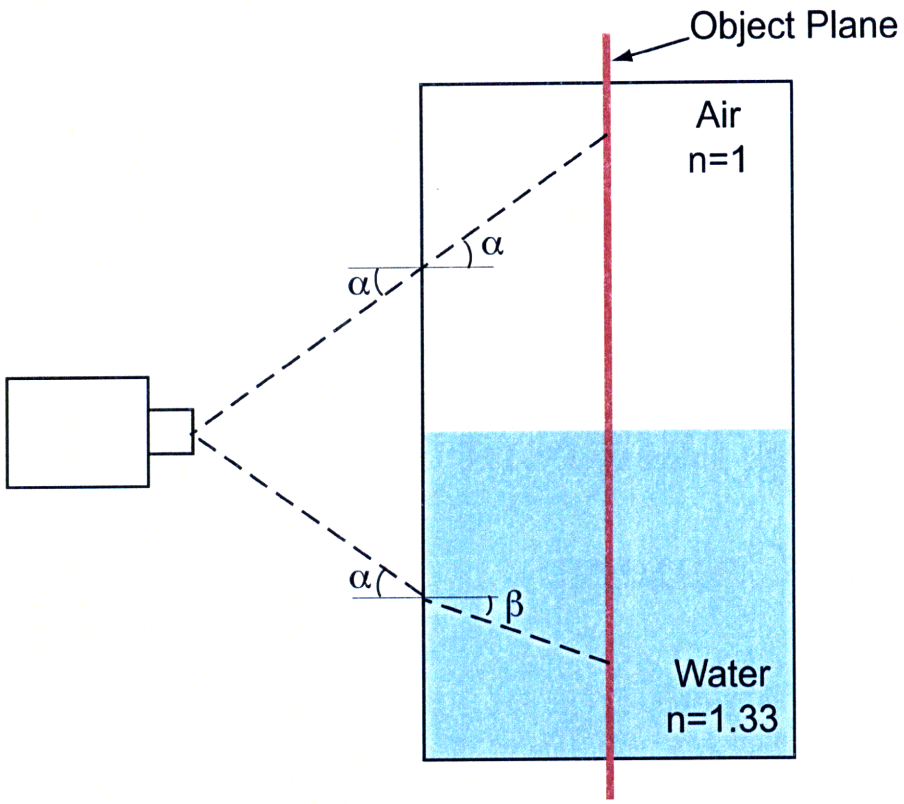

Figure B-1: Schematic of how index of refraction effectively changes the FOV of an imaging system.

where $n_{water} = 1.33$ and $n_{air} = 1$. Since $n_{water} > n_{air}$, Snell's Law requires $sin\beta < sin\alpha$, and therefore $\beta < \alpha$. Thus, the effective angular acceptance of light rays emanating from the water is less than that for air, and the same camera will see a smaller FOV in water.

Bibliography

[1] R. J. Adrian. Twenty years of particle image velocimetry. *Exp. Fluids*, 39:159–169, July 2005.

[2] Ronald J. Adrian. Particle-imaging techniques for experimental fluid mechanics. *Annu. Rev. Fluid Mech*, 23:261–304, 1991.

[3] M. L. Banner and W. K. Melville. On the separation of air flow over water waves. *J. Fluid Mech*, 77:825–842, October 1976.

[4] Hector D. Ceniceros and Thomas Y. Hou. Dynamic generation of capillary waves. *Phys. Fluids*, 11(5):1042–1050, May 1999.

[5] Kuang-An Chang and Philip L.-F. Liu. Experimental investigation of turbulence generated by breaking waves in water of intermediate depth. *Phys. Fluids*, 11(11):3390–3400, November 1999.

[6] David Joel Chen. Designing wave–measuring instruments. *MIT Master's Thesis*, May 1994.

[7] Gang Chen, Christian Kharif, Stephane Zaleski, and Jie Li. Two-dimensional navier-stokes simulation of breaking waves. *Phys. Fluids*, 11(1):121–133, January 1999.

[8] Dana Dabiri and Morteza Gharib. Experimental investigation of the vorticity generation within a spilling water wave. *J. Fluid Mech*, 330:113–139, January 1997.

[9] Pierre-Gilles de Gennes, Françoise Brochard-Wyart, and David Quéré. *Capillarity and Wetting Phenomena: Drops, Bubbles, Pearls, Waves.* Springer Science + Business Media, LLC, New York, NY, 2004.

[10] James H. Duncan. Spilling breakers. *Annu. Rev. Fluid Mech*, 33:519–47, January 2001.

[11] James H. Duncan, Haibing Qiao, Vasanth Philomin, and Alexandra Wenz. Gentle spilling breakers: Crest profile evolution. *J. Fluid Mech*, 379:191–222, January 1999.

[12] Richard S. Figliola and Donald E. Beasley. *Theory and Design for Mechanical Measurements, Third Edition.* John Wiley & Sons, Inc., USA, 200.

[13] Kelli L. Hendrickson. *Navier-Stokes Simulation of Steep Breaking Water Waves with a Coupled Air-Water Interface.* PhD thesis, MIT, February 2005.

[14] Joseph O. Hirschfelder, Charles F. Curtiss, and R. Byron Bird. *Molecular Theory of Liquids and Gases.* John Wiley & Sons, Inc., USA, 1954.

[15] A. T. Hjelmfelt, Jr. and L. F. Mockros. Motion of discrete particles in a turbulent fluid. *Appl. Sci. Res*, 16(1):149–161, January 1966.

[16] Winslow Homer. Incoming tide, scarboro maine, 1883.

[17] H Huang, D Dabiri, and M Gharib. On errors of digital particle image velocimetry. *Meas. Sci. Technol.*, 8:1427–1440, 1997.

[18] Sanshiro Kawai. Structure of air flow separation over wind wave crests. *Boundary-Layer Meteorol*, 23:503–521, August 1982.

[19] KRUSS. 1020 Crews Road, Suite K, Matthews, NC 28105, USA. www.kruss.info. Personal Communication.

[20] J. C. Lin and D. Rockwell. Evolution of a quasi-steady breaking wave. *J. Fluid Mech*, 302:29–44, November 1995.

[21] Michael. S. Longuet-Higgins. On wave breaking and the equilibrium spectrum of wind–generated waves. *Proc. Roy. Soc. A.*, 310:151–159, 1969.

[22] Michael. S. Longuet-Higgins. Capillary rollers and bores. *J. Fluid Mech*, 240:659–679, 1992.

[23] Michael. S. Longuet-Higgins. Shear instability in spilling breakers. *Proceedings: Mathematical and Physical Sciences*, 446:399–409, 1994.

[24] Michael. S. Longuet-Higgins and E. D. Cokelet. The deformation of steep surface waves on water. i. a numerical method of computation. *Proc. R. Soc. London. A*, 350:1–26, 1976.

[25] Angus Kai McDonald. Experimental investigation of small-scale breaking waves: Flow visualization across the air-water interface. *MIT Master's Thesis*, May 2005.

[26] A Melling. Tracer particles and seeding for particle image velocimetry. *Meas. Sci. Technol.*, 8(12):1406–1416, December 1997.

[27] W. K. Melville. The role of surface-wave breaking in air-sea interaction. *Annu. Rev. Fluid Mech*, 28:279–321, January 1996.

[28] W. Kendall Melville, Fabrice Veron, and Christopher J. White. The velocity field under breaking waves: Coherent structures and turbulence. *J. Fluid Mech*, 454:203–233, March 2002.

[29] J. N. Newman. *Marine Hydrodynamics.* The MIT Press, Cambridge, MA, 1977.

[30] William L. Peirson. Measurement of surface velocities and shears at a wavy air-water interface using particle image velocimetry. *Exp. Fluids*, 23(5):427–437, November 1997.

[31] D. H. Peregrine. Breaking waves on beaches. *Annu. Rev. Fluid Mech*, 15:149–178, 1983.

[32] Marc Perlin, Jianhui He, and Luis P. Bernal. An experimental study of deep water plunging breakers. *Phys. Fluids*, 8(9):2365–2374, September 1996.

[33] Haibing Qiao and James H. Duncan. Gentle spilling breakers: Crest flow-field evolution. *J. Fluid Mech*, 439:57–85, July 2001.

[34] Markus Raffel, Christian E. Willert, and Jurgen Kompenhans. *Particle Image Velocimetry: A Practical Guide.* Springer-Verlag, Berlin Heidelberg, 1998.

[35] R. J. Rapp and W. K. Melville. Laboratory measurements of deep-water breaking waves. *Phil. Trans. R. Soc. Lond.*, 331(1622):735–800, June 1990.

[36] Nicolas Reul, Hubert Branger, and Jean-Paul Giovanangeli. Air flow structure over short-gravity breaking water waves. *Boundary-Layer Meteorol*, 126:477–505, March 2008.

[37] Subramanian V. Sankar, Derek Y. Kamemoto, and William D. Bachalo. Sizing large hollow micro-balloons with the phase doppler interferometer. *Part. Part. Syst. Charact.*, 10:321–331, December 1993.

[38] M. H. Kamran Siddiqui and Mark R. Loewen. Characteristics of the wind drift layer and microscale breaking waves. *J. Fluid Mech*, 573:417–456, February 2007.

[39] M. Stanislas, K. Okamoto, C.J. Kahler, and J. Westerweel. Main results of the second international piv challenge. *Exp. Fluids*, 39:170–191, 2005.

[40] Ib A. Svendsen. *Introduction to Nearshore Hydrodynamics.* World Scientific, Toh Tuck Link, Singapore, 2006.

[41] Marshall P. Tulin. Breaking of ocean waves and downshifting. In John Grue, Bjørn Gjevik, and Jan Erik Weber, editors, *Waves and Nonlinear Processes in Hydrodynamics*, pages 177–190. Kluwer Academic Publishers, Dordrecht, The Netherlands, 1996.

[42] F. Veron, G. Saxena, and S. K. Misra. Measurements of the viscous tangential stress in the airflow above wind waves. *Geophys. Res. Lett.*, 34, October 2007.

[43] J Westerweel. Fundamentals of digital particle image velocimetry. *Meas. Sci. Technol.*, 8:1379–1392, 1997.

[44] J Westerweel. Theoretical analysis of the measurement precision in particle image velocimetry. *Exp. Fluids*, [Suppl.]:S3–S12, 2000.

[45] C. E. Willert and M. Gharib. Digital particle image velocimetry. *Exp. Fluids*, 10:181–193, 1991.